Ozone vegetation damage effects on gross primary productivity in the United States

Xu Yue and Nadine Unger
School of Forestry and Environmental Studies, Yale University, 195 Prospect Street, New Haven, CT 06511
Correspondence to: Xu Yue (xu.yue@yale.edu)

Abstract

We apply an off-line process-based vegetation model (the Yale Interactive Terrestrial Biosphere model) to assess the impacts of ozone (O_3) vegetation damage on gross primary productivity (GPP) in the United States during the past decade (1998-2007). The model's GPP simulation is evaluated at 40 sites of the North American Carbon Program (NACP) synthesis. The ecosystem-scale model version reproduces interannual variability and seasonality of GPP at most sites, especially in croplands. Inclusion of the O_3 damage impact decreases biases of simulated GPP at most of the NACP sites. The simulation with the O_3 damage effect reproduces 64% of the observed variance in summer GPP and 42% on the annual average. Based on a regional gridded simulation over the U.S., summertime average O_3-free GPP is 6.1 g C m^{-2} day^{-1} (9.5 g C m^{-2} day^{-1} in the East of 95°W and 3.9 g C m^{-2} day^{-1} in the West). O_3 damage decreases GPP by 4-8% on average in the eastern U.S. and leads to significant decreases of 11-17% in east coast hotspots. Sensitivity simulations show that a 25% decrease in surface O_3 concentration halves the average GPP damage to only 2-4%, suggesting the substantial co-benefits to ecosystem health that may be achieved via O_3 air pollution control.

Keywords: Ozone, gross primary productivity, photosynthesis, stomatal conductance

1 Introduction

The effects of tropospheric ozone (O_3) damage on U.S. forests have been studied for half a century (Karnosky et al., 2007), but the impacts of O_3 on the North American carbon balance are still relatively poorly understood (Felzer et al., 2004; Huntingford et al., 2011). O_3 is a secondary pollutant produced in the troposphere during the photochemical oxidation of carbon monoxide, methane, and volatile organic compounds (VOCs) by the major tropospheric oxidant, the hydroxyl radical, in the presence of sunlight and nitrogen oxides. Fossil-fuel, biofuel and biomass burning since the industrial and agricultural revolutions have greatly increased the emissions of O_3 precursors and led to an approximate doubling of O_3 levels over the U.S. since the preindustrial. Deposition through stomatal uptake is an important sink for O_3 but damages photosynthesis, reduces plant growth and biomass accumulation, limits crop yields, and affects stomatal control over plant transpiration of water vapor between the leaf surface and atmosphere (Ainsworth et al., 2012; Hollaway et al., 2012).

Understanding the O_3 pollution influence on the North American forest sink is crucial to any effort to mitigate climate change by stabilizing atmospheric carbon dioxide (CO_2) concentrations. Currently, North America is acting as a net source of CO_2 to the atmosphere (King et al., 2012), mainly due to fossil-fuel combustion in the U.S. and the deforestation in Mexico. Sequestration of atmospheric CO_2 by forest ecosystems is a major control on atmospheric CO_2 abundance and its growth rate (Pan et al., 2011). Terrestrial ecosystems of North America absorb the equivalent of about 35% of North America's fossil fuel based CO_2 emissions, representing a source-to-sink ratio of nearly 3:1. Forest regrowth in the U.S. is responsible for 30–70% of this North American CO_2 sink, which varies significantly from year to year (Pacala et al., 2001; Goodale et al., 2002; Pan et al., 2011; King et al., 2012). However, O_3 damage may in part dampen the level of carbon sequestration by North American ecosystems (Felzer et al., 2004; 2005).

Experimental studies that examine O_3 impacts on plant productivity are typically performed for individual vegetation types, on the scale of sites, and within a limited time

period (e.g. Wittig et al., 2007; Feng et al., 2008; Lombardozzi et al., 2013). For example, based on measurements reported from over 100 studies, Wittig et al. (2007) estimated that chronic O_3 exposure depressed photosynthesis by 11% and stomatal conductance by 13% for several tree species at the ambient O_3 level of ~45 ppbv relative to that in O_3-free air. The O_3 damage effect is strongest for crops. With datasets from ~50 peer-reviewed studies, Feng et al. (2008) estimated that elevated O_3 levels significantly decrease wheat photosynthetic rates by 20% and stomatal conductance by 22%. Emerging research has found that the O_3 vegetation damage effects may result in a loss of plant stomatal control, and a consequent decoupling of the stomatal response from photosynthesis inhibition (Lombardozzi et al., 2012a, 2012b, 2013).

Previous work has found that in the U.S. region during 1989-1993, O_3 pollution reduced net primary productivity (NPP) by 3-7% overall, and up to 13% in hotspots including the southeast and in the Midwest agricultural lands (Felzer et al., 2004, 2005). The indirect CO_2 radiative forcing due to the vegetation damage effects of anthropogenic O_3 increases since the industrial revolution may be as large as +0.4 Wm^{-2} (Sitch et al., 2007), which is 25% of the magnitude of the direct CO_2 radiative forcing over the same period, and of similar magnitude to the direct O_3 radiative forcing. Through this perturbation of the carbon cycle, O_3 pollution affects the climate system on considerably longer timescales than its own atmospheric lifetime (Unger and Pan, 2012). Over the past decade since this previous assessment surface O_3 levels in most of the U.S. have decreased (Lefohn et al., 2010) due to domestic emission reductions following the implementation of air quality control legislation (Bloomer et al., 2010). However, increasing O_3 concentration is observed over western U.S. (Jaffe and Ray, 2007). Such a trend may in part be related to the inter-continental flow from Asia (Cooper et al., 2010) and the global increase in methane (Rigby et al., 2008).

The major goal of this study is to assess O_3 damage effects on gross primary productivity (GPP) in the U.S. for the recent decade 1998-2007 using a data-constrained vegetation model. In this work, we describe the implementation of a semi-mechanistic O_3 damage function (Sitch et al., 2007) into the **Y**ale **I**nteractive Terrestrial **B**io**s**phere model (YIBs)

93 that includes enzyme-kinetic biophysics (Unger et al., 2013). In the first stage of the
94 study, we utilize eddy-derived GPP flux measurements at 40 sites across the U.S. and
95 Canada that have been collated for the North American Carbon Program (NACP) site-
96 level interim synthesis (Huntzinger et al., 2012; Schaefer et al., 2012; Barr et al., 2013;
97 Ricciuto et al., 2013) to evaluate an off-line version of the vegetation model's site level
98 GPP simulation and to assess the impact of surface O_3 damage at those sites. In the
99 second stage of the study, the impacts of O_3 damage on GPP throughout the entire U.S.
100 are quantified using a regional configuration of the vegetation model.
101
102 **2 Methodology and data**
103
104 **2.1 Vegetation biophysics**
105
106 Here, we apply an off-line version of the YIBs model that previously was implemented
107 into the NASA Goddard Institute for Space Studies global chemistry-climate model
108 (Unger et al., 2013). The off-line model can be run at the site-level or in regional mode
109 for a designated region. The vegetation biophysics module computes the photosynthetic
110 uptake of CO_2 coupled with the transpiration of water vapor at the 1-hour physical
111 integration time step of the off-line model. The vegetation biophysics calculates C3 and
112 C4 photosynthesis using the well-established Michealis-Menten enzyme-kinetics leaf
113 model of photosynthesis (Farquhar et al., 1980; von Caemmerer and Farquhar, 1981) and
114 the stomatal conductance model of Ball and Berry (Collatz et al., 1991). The coupled
115 photosynthesis/stomatal conductance leaf model has been widely used to project
116 terrestrial biosphere responses to global change. The model is briefly summarized here
117 for transparency and completeness. The leaf model assumes that the rate of net CO_2
118 assimilation (A_{net}) in the leaves of C3 and C4 plants is limited by one of three processes:
119 (i) the capacity of the ribulose 1,5-bisphosphate (RuBP) carboxylase-oxygenase enzyme
120 (Rubisco) to consume RuBP (J_c); (ii) the capacity of the Calvin cycle and the thylakoid
121 reactions to regenerate RuBP supported by electron transport (J_e); (iii) the capacity of
122 starch and sucrose synthesis to consume triose phosphates and regenerate inorganic
123 phosphate for photo-phosphorylation in C3 and phosphoenolpyruvate (PEP) limitation in

C4 (J_s). J_c, J_e, and J_s are described as functions of the maximum carboxylation capacity (V_{cmax}) at the optimal temperature, 25°C, and the internal leaf CO_2 concentration (C_i). The gross rate of carbon assimilation from photosynthesis (A) is given by:

$$A = \min(J_c, J_e, J_s) \quad (1)$$

Net carbon assimilation is given by:

$$A_{net} = A - R_d \quad (2)$$

where R_d is the rate of dark respiration:

$$R_d = 0.015 \cdot V_{c\max} \quad (3)$$

Leaf stomata control the uptake of CO_2 versus the loss of H_2O. At equilibrium, the stomatal conductance of water vapor through the leaf cuticle (g_s in mol [H_2O] m^{-2} s^{-1}) depends on the net rate of carbon assimilation:

$$g_s = m\frac{A_{net} \cdot RH}{c_s} + b = \frac{1}{r_s} \quad (4)$$

where m and b are the slope and intercept derived from empirical fitting to the Ball and Berry stomatal conductance equations, RH is relative humidity, c_s is the CO_2 concentration at the leaf surface, and r_s is the stomatal resistance to water vapor. Appropriate photosynthesis parameters for the local vegetation type are taken from (Friend and Kiang, 2005) and the Community Land Model (Oleson et al., 2010) with updates from Bonan et al. (2011) (Table 1). In both the site-level and regional models, we apply these model PFT-specific photosynthesis parameters and do not tune or calibrate to the local vegetation properties. The model calculates evapotranspiration as a function of the stomatal conductance. However, we do not consider the feedback of the changes in evapotranspiration to the boundary-layer meteorology because we use prescribed meteorological variables from reanalysis in the simulations.

The canopy radiative transfer scheme assumes a closed canopy and layers the canopy for light stratification using an adaptive number of layers (typically 2-16) (Friend and Kiang, 2005). Each canopy layer distinguishes sunlit and shaded regions for which the direct and diffuse photosynthetically active radiation (PAR) is computed (Spitters et al., 1986). The coupled photosynthesis and stomatal conductance equations are solved analytically using a cubic function of A_{net}. C_i is calculated explicitly at the leaf level. Scaling of the leaf to

canopy level is through stratification of canopy light levels and leaf area profiles. The photosynthetic uptake of CO_2 is accumulated into a carbon reserve pool, from which other processes may allocate uses.

2.1.1 O_3 damage effect on photosynthesis

O_3 oxidizes cellular membranes and photosynthetic tissues when it enters leaves through stomata, leading to reductions in photosynthesis and GPP. O_3 damage inhibits stomatal conductance, which is closely related to the photosynthetic rate, resulting in a reduction in transpiration. A semi-mechanistic parameterization is employed to estimate the O_3 damage effects to both photosynthesis and stomatal conductance (Sitch et al., 2007). The exposure to O_3 leads to reductions in photosynthesis:

$$A' = F \cdot A_{net} \tag{5}$$

where F is the reduction fraction calculated as

$$F = 1 - a \cdot U_{>O3T} \tag{6}$$

where a is the O_3 sensitivity coefficient derived from observations. Two cases are examined: high and low O_3 sensitivity following Sitch et al. (2007). $U_{>O3T}$ is the instantaneous leaf uptake of O_3 flux above a plant function type (PFT)-specific threshold of O3T (Table 1),

$$U_{>O3T} = \max[(F_{O3} - O3T), 0] \tag{7}$$

here F_{O3} is the O_3 flux entering the leaf through the stomata,

$$F_{O3} = \frac{[O_3]}{r_b + \kappa \cdot r_s'} \tag{8}$$

where $[O_3]$ is the O_3 concentration at the top of the canopy, r_b is the boundary layer resistance. The stomatal resistance to O_3 is calculated based on stomatal resistance to water r_s with a ratio constant κ=1.67. From Equation (4), the decrease in A_{net} reduces the stomatal conductance g_s proportionally,

$$r_s' = \frac{1}{g_s'} = \frac{1}{F \cdot g_s} \tag{9}$$

The r_s' and g_s' are the O_3-damaged stomatal resistance and conductance, respectively. When the plant is exposed to [O_3] (Equation 8), the excess O_3 flux entering leaves (Equation 7) causes $F<1$ (Equation 6), decreasing A_{net} (Equation 5) while increasing the stomatal resistance (Equation 9). The latter will act to reduce the O_3 uptake flux (Equation 8) to protect the plant. Thus, the scheme considers associated changes in both photosynthetic rate and stomatal conductance. When photosynthesis is inhibited by O_3, the stomatal conductance decreases accordingly to resist more air passing through the stomata, resulting in a decline of the oxidant fluxes inside leaves, as described through equations (5)-(9). Consequently, this coupled scheme represents the equilibrium state between the CO_2 demand for vegetation growth and the protection against O_3 damage by plant. The parameters for the scheme, including the O_3 damage threshold and sensitivity coefficients, were originally derived based on the calibration of the MOSES vegetation model. Since the MOSES model employs the (almost) identical Farquhar-Ball-Berry photosynthesis/stomatal conductance scheme as in the YIBs model, it is appropriate to adopt the same parameters as those derived in Sitch et al. (2007) (Table 1). Evaluation of the YIBs simulated O_3-induced GPP response with available field and laboratory measurements across a range of PFTs in Section 3.4 indicates that our assumption is reasonable.

2.1.2 Vegetation structure

The YIBs vegetation model simulates eight PFTs, using either C3 or C4 photosynthesis (Table 1). We apply two different sets of land cover and leaf area index (LAI) in the simulations. The first set is the PFT-specific vegetation cover fraction and LAI retrieved by the Moderate Resolution Imaging Spectroradiometer (MODIS, Knyazikhin et al., 1998). The value on a specific day is linearly interpolated from the monthly means of the nearest two months based on the distance of this day to the middle dates of those two months. The second set uses LAI from the Global Modeling and Assimilation Office (GMAO) Modern Era-Retrospective Analysis (MERRA) dataset. The MERRA LAI is assimilated based on radiance data retrieved by over 20 satellites (Rienecker et al., 2011) and is available on a daily scale from 1980 onwards. Since the MERRA LAI dataset does

not provide PFT-specific information, the actual site-level PFT is assumed for the site level simulations. For the regional simulations, the land cover is prescribed to the gridded International Satellite Land-Surface Climatology Project (ISLSCP, Hall et al., 2006).

2.1.3 Meteorological forcing

For the site-level simulations, we use hourly *in situ* measurements of surface meteorological variables, including surface air temperature, specific humidity, wind speed, surface pressure, and CO_2 concentrations. There are some missing values in the measurements due to occasional instrument failure. We gap-fill the site-based observations with that from the MERRA-land data (Reichle et al., 2011), which is interpolated to each site based on the site location.

For the regional simulations, the off-line YIBs model uses hourly MERRA-land data climatic variables including: surface air temperature, specific humidity, wind speed, surface pressure, precipitation, direct PAR, and diffuse PAR, and soil temperature and soil moisture at 6 soil depths. The original data resolution of 0.5°×0.667° by latitude and longitude is degraded to 1°×1.333° due to current disk space limitation.

2.1.4 Surface [O_3]

Hourly and daily maximum 8-hour average surface [O_3] representative of the present day climate (~ 2005) are taken from previous simulations using NASA Model-E2 (Shindell et al., 2013). The global model has 2°×2.5° latitude by longitude horizontal resolution with 40-vertical layers extending to 0.1 hPa. The gas-phase chemistry and aerosol modules are fully integrated, so that these components interact with each other and with the physics of the climate model (Bell et al., 2005; Shindell et al., 2006; Unger, 2011; Shindell et al., 2013). The model surface O_3 is validated using measurements from 73 Clean Air Status and Trends Network (CASTNET) sites operated by the Unitied States Environmental Protection Agency (EPA) (http://epa.gov/castnet/javaweb/ozone.html) and ~1200 monitor sites managed by the EPA AIRDATA (http://www.epa.gov/airdata/). These sites

are operated on the county level scale. The CASTNET provides hourly [O_3] at rural sites from 1996-2005. The AIRDATA network provides daily maximum 8-hour average (MDA8) [O_3], covering both urban and rural regions. We use AIRDATA data for the year 2005.

2.2 Simulations

2.2.1 Site-level runs

We configure a site-level version of the YIBs model for the 40 eddy covariance flux tower sites described in detail in the NACP synthesis (Fig. S1 and Appendix Table A, Schaefer et al., 2012). Meteorological measurements are available for a wide range of time periods across the different sites ranging from the minimum of 1 year at Fermi Lab (US-IB1) and the maximum of 15 years at Harvard Forest (US-HA1). These sites cover a range of different vegetation types including: evergreen needleleaf forest (ENF), deciduous broadleaf forest (DBF), grasslands, croplands, closed shrublands, mixed forests, permanent wetlands, and woody savannas. Table S1 summarizes how the NACP vegetation types are mapped onto the 8 model PFTs. For the site-level simulations, we assume C4 photosynthetic pathway for all cropland sites, which are mainly corn (Schaefer et al., 2012). The local site LAI values are not available. As a result, we use the MERRA or MODIS LAI for the simulations.

For each site, a group of six sensitivity simulations are performed (Table 2). We conduct the first four runs using different combinations of meteorological and vegetation forcings, to assess the sensitivity of the results to local versus renalaysis meterological forcing and LAI (Table 2). Two, METmerra_LAImodis and METmerra_LAImerra, use hourly meteorology from MERRA-land reanalyses alone. The other two, METsite_LAImodis and METsite_LAImerra, use site-based meteorology with gap-filled MERRA reanalysis. Simulations use two datasets of LAI: (1) METmerra_LAImerra and METsite_LAImerra use LAI from the MERRA-land reanalyses, which provide non PFT-specific LAI that we assign to the local PFT type at each site (Table A), while (2) METmerra_LAImodis and

METsite_LAImodis use PFT-specific LAI retrieved by the MODIS. Later analyses show that METsite_LAImerra has the lowest biases relative to other O_3-free simulations. We perform two additional site-level simulations, which use the same forcings as that for METsite_LAImerra but with the impact of O_3 uptake on photosynthesis. These two experiments, METsite_LAImerra_HO3 and METsite_LAImerra_LO3, use either high or low O_3 sensitivity as defined by the coefficient *a* in Table 1.

To quantify the performance of the vegetation model, we estimate the χ^2 for each site following the method described in Schaefer et al. (2012),

$$\chi^2 = \frac{1}{n}\sum_{i=1}^{n}\left(\frac{r_i}{\varepsilon_i}\right)^2 \tag{10}$$

where

$$r_i = \left(GPP_{si} - GPP_{oi}\right) \tag{11}$$

is the difference between the pair of simulated and observed GPPs. ε_i are the observational uncertainties resulting from turbulence, gap-filling, flux partitioning, and u* threshold determination (Barr et al., 2013). *n* is the length of observations (e.g. the number of days for the daily variables). The lower the χ^2, the smaller the model biases. If $\chi^2 < 1$, the simulation bias is on average smaller than the measurement uncertainty, indicating a good performance of the model. Here, we define a reasonable performance of $\chi^2 < 4$, when the residual is less than twice the measurement uncertainty. We also calculate the root mean square error (RMSE) as follows:

$$RMSE = \sqrt{\frac{1}{n}\sum_{i=1}^{n}\left(GPP_{si} - GPP_{oi}\right)^2} \tag{12}$$

We validate the simulated O_3 damage effect with measurements from literature. Field and laboratory experiments may have different [O_3] compared to the ambient level we used complicating the validation. As a result, we perform 14 additional sensitivity simulations for each of NACP sites. All tests use meteorological and vegetation forcings the same as METsite_LAImerra (Table 2), except for the different [O_3] and O_3 sensitivity. These

experiments are divided into two groups, 7 in each, using either low or high O_3 sensitivity. In each group, simulations are performed with constant [O_3] at 20, 40, 60, 80, 100, 120, 140 ppbv, respectively. We do not include diurnal and seasonal variations of [O_3] in these sensitivity simulations as that in METsite_LAImerra for two reasons. First, field measurements for the O_3 vegetation damage are usually performed with fixed [O_3] during the growth season (e.g. Ishii et al., 2004; Zhang et al., 2012). Second, the diurnal cycles and seasonality of [O_3] are very different for different sites (Bloomer et al., 2010), making it difficult to apply a uniform temporal cycle for all the NACP sites. The reductions in GPP at these simulations are compared with results from field measurements at the corresponding [O_3] level.

2.2.2 Regional run over U.S.

A gridded version of the YIBs model at 1°×1.333° latitude by longitude horizontal resolution for the U.S. region is driven with MERRA meteorological forcings for the period 1998-2007. In the regional model, vegetation cover types are from the ISLSCP and LAI is form the MERRA-land reanalysis. We assign the MERRA LAI to the corresponding PFT types defined by ISLSCP (Fig. S2). The 18 ISLSCP land types are converted to 8 PFTs used in the model (Table S1). Some of the ISLSCP land types, such as the deciduous needleleaf forest, are not represented in the YIBs model. However, the coverage of these types is very small in the U.S. (Fig. S2) and will not influence the regional simulation after the conversion to the model types. For the regional simulation, we assume that the total crop area in each crop grid cell is split 50% C3 and 50% C4 to account for the dominance of both soybean (C3) and corn (C4) crops in the central and northern U.S. agricultural regime. We perform 2 simulation cases with high and low O_3 damage sensitivity. Finally, to understand how the O_3 vegetation damage effect may respond to possible future changes in [O_3], we perform four additional sensitivity experiments with ±25% changes in [O_3] for each O_3 sensitivity case.

3. Results and discussion

3.1 Evaluation of O_3-free GPP at NACP sites

We first compare the monthly mean LAI from MERRA and MODIS at each NACP site (Fig. S3). For each site, the MERRA LAI is averaged for the period when GPP measurements are available. The two datasets show similar annual cycles at several sites but are inconsistent for 7 out of 20 ENF sites (CA-Ca1, CA-Ca2, CA-Ca3, CA-NS1, US-Me2, US-Me3, and US-Me5) and 2 out of 5 shrubland sites (US-SO2 and US-Ton). In addition, for grasslands and croplands, the datasets exhibit different seasonality. It must be emphasized that the MERRA and MODIS LAI represent the average state in the retrieval product grid cells and as such may not represent the local LAI for the actual PFT species at each site.

The long-term monthly mean O_3-free GPP from the simulation METsite_LAImerra is compared with observations at NACP sites (Fig. 1 and Fig. S4). The simulations capture the magnitude and seasonality of GPP for most sites especially for deciduous broadleaf and cropland. The largest model overestimate (factor of 3-8) occurs at two ENF sites, CA-SJ1 and CA-SJ2 in North Central Canada (Fig. S4). For the grassland sites, the model-observation correlation is low because the seasonality is not well captured, especially for US-ARM (in Great Plains) and US-Var (in California), where the modeled maximum GPP occurs in summer (July), 2-3 months later than in the measurements (April) (Fig. S4). This incorrect model seasonality is a result of the MERRA LAI (compare Fig. S3) that does not begin to increase rapidly until after May and is not consistent with the local LAI at the site. In reality, California grasslands exhibit rapid growth in spring then mature and die after April or May (Chiariello, 1989). The grasslands in the Great Plains may have up to six different phenological groups, including some species active in spring (e.g. in US-ARM) while some others peak in summer (e.g. in US-Shd) (Henebry, 2003). On the annual mean basis, the correlation coefficient between simulated GPP and observations at all 40 sites is 0.65. The correlation is higher (0.81) for summer (June-August, Fig. S5). The annual GPP averaged over all 40 sites is 3.8 g C m^{-2} day^{-1}, 27% higher than the observational average (3.0 g C m^{-2} day^{-1}).

Among the 40 NACP sites, 22 have reasonable performance with $\chi^2 < 4$ for the simulation METsite_LAImerra (Fig. 2a). For these sites, 12 are ENF with the best (χ^2 =1.2) at site US-Dk3 (Fig. S4). The ENF sites usually have multiple years of measurements and provide good samples for testing the consistency between simulations and observations. Simulations at other 4 DBF, 3 cropland, and 3 shrubland sites have $\chi^2 <$ 4. Compared with the 24 land surface models in Schaefer et al. (2012), the YIBs model shows significant improvement at the crop PFT sites ($\chi^2 < 4.1$ vs. $\chi^2 > 6$). YIBs simulates GPP with $\chi^2 < 4$ at 22 sites in total compared to 16 sites for the ensemble simulations in Schaefer et al. (2012). YIBs GPP simulation is weaker ($\chi^2 > 4$) at 18 sites including 8 ENF, 2 DBF, and 2 shrubland PFTs. The common feature of the biases at these sites is the overestimation of peak GPP during summer (e.g. CA-SJ1, CA-SJ2, CA-Mer, Fig. S4). It is possible that the model does not represent the full realism of the biophysical processes accurately. However, we assert that the most likely cause of the model overestimate is the uniform application of model PFT-specific photosynthesis parameters that are not tuned to local site level vegetation parameters and, for instance, do not take into account plant species and age. Similar to the multi-model results in Schaefer et al. (2012), YIBs performance is weakest at the 5 grassland sites. In this case, the bias is mainly due to the delayed LAI seasonality in the MERRA satellite dataset (Figs. S3 and S4). In general, application of the remotely sensed LAI is a source of error because the gridded satellite data may not represent the local site changes in plant growth and phenology, especially for vegetation types with low biomass. The limitation of the satellite LAI spatial resolution implies that the model is unable to resolve GPP variability for sites in close proximity. For example, sites CA-SJ1, CA-SJ2, and CA-SJ3 are located close to each other. Simulations at these sites have similar magnitude in simulated GPP while observations show distinct variability between the sites.

We compare R^2, RMSE, and χ^2 for the different sensitivity experiments in order to ascertain which combination of meteorological and LAI forcings best reproduces the measured GPP over North America (Table 3 and Fig. 3). CA-Let, CA-NS1, US-Var, CA-SJ1, and CA-SJ2 are excluded from the analysis because of the excessive bias at those sites (Fig. S6a). The average R^2 increases while RMSE decreases when MERRA

reanalyses are substituted with site-based meteorology, or the MERRA LAI is used instead of MODIS LAI (Table 3). The choice of LAI forcing has the most significant impact on YIBs simulation performance, consistent with previous work that showed the dominance of phenology over meteorology in controlling local terrestrial carbon exchange (Desai et al., 2008; Puma et al., 2013). Using MODIS LAI, YIBs has a total χ^2 of 9.2 that shows an average reduction of 4.7 (52%) with MERRA LAI (Table 3 and Fig. 3). Applying the site meteorology relative to MERRA meteorological forcings offers smaller improvements. For example, the total χ^2 value decreases by 5% in METsite_LAImodis compared with that in METmerra_LAImodis and 15% in METsite_LAImerra relative to that in METmerra_LAImerra (Table 3).

3.2 Evaluation of modeled surface [O_3]

We validate summertime surface O_3 simulated by the NASA Model-E2 chemistry-climate model with observations from the CASTNET and AIRDATA (Fig. 4). High O_3 level appears in the eastern U.S. due to anthropogenic emissions and in the mountainous western U.S. due to high elevation. The model generally captures this spatial pattern with a correlation coefficient of 0.39 against observations over the selected 73 CASTNET sites (Figs. 4a-b). The simulation overestimates the O_3 level by ~4 ppbv (12%) in the East and ~1 ppbv (3%) in the West. The CASTNET sites are located in rural sites, which usually have lower [O_3] than that in urban areas, except for some megacities where the excessive NO_x emissions result in lower O_3 level (Gregg et al., 2003). Therefore, we also compare the simulated MDA8 [O_3] with monitored at ~1200 AIRDATA sites, which covers both urban and rural regions (Fig. 4c). In the eastern U.S., the model captures high [O_3] centers around Michigan, Indiana, and Ohio states and that along the northeast coast. In the West, the simulation reproduces high [O_3] over mountain regions and in California. On average, the simulated MDA8 [O_3] is lower by ~0.5 ppbv (1%) in the East and ~3.5 ppbv (7%) in the West. The correlation coefficient between simulations and observations is as high as 0.51 (Fig. 4d).

3.3 O_3 damage effects at NACP sites

We must apply the simulated O_3 to quantify the O_3 vegetation damage at the NACP sites because the sites do not monitor local [O_3]. The summer average [O_3] is 30-50 ppbv at 24 U.S. sites (Fig. 5a). The O_3 damage effect is relatively stronger at sites with both high O_3-free GPP and ambient [O_3] (Fig. 5d). The most significant damages are predicted at US-MMS (DBF) and US-Dk3 (ENF) sites, where the GPP reductions are 5-14% depending on the low or high O_3 sensitivity (Fig. 5d). At these two sites, the high stomatal conductance (4.0 and 3.4 mm s^{-1}, Fig. 5b) and ambient [O_3] (both 43 ppbv, Fig. 5a) result in the largest O_3 stomatal flux (both ~0.3 mmol m^{-2} d^{-1}, Fig. 5c) among the 24 sites. The lowest O_3 damage (1-2% GPP reduction) appears in the 3 shrub sites, US-Ton, US-SO2, and US-Los, although mean [O_3] there is as high as 43 ppbv. The main reason for the limited O_3 damage is the low stomatal conductance (average 1.4 mm s^{-1}, Fig. 5b) related to the small O_3-free GPP (average 4.6 g C m^{-2} d^{-1}, Fig. 5d). Similarly, the O_3 damage for C3 grass is as low as 1-2%, although the GPP of this plant is highly sensitive to O_3 (Table 1). For ENF and DBF sites, the average site-level O_3 damage effects are estimated to be 2-5% and 3-9% respectively with differences between these ecosystem types predominantly driven by differences in sensitivity to O_3. The four C4 crop sites, US-Ne1, US-IB1, US-Ne2, and US-Ne3, exhibit the highest O_3-free GPP but show only moderate O_3 damage effects (GPP reductions of 4-6%, Fig. 5d). This result is driven by low ambient [O_3] at the C4 crop sites (average 32 ppbv, Fig. 5a) in combination with the reduced C4 stomatal conductance (higher water use efficiency) relative to C3 plants (average 3.2 mm s^{-1}, Fig. 5b). Indeed, the C4 photosynthetic pathway has been observed to offer protection against O_3 damage (Heagle et al., 1989; Rudorff et al., 1996).

Inclusion of O_3 damage effect improves the site-level simulations (Figs. 2b-c). For 36 out of the 40 sites, the χ^2 of simulated GPP decreases when considering vegetation responses to O_3, and the improvement is better when higher O_3 sensitivity is applied. At these sites, for example, CA-TP4, US-Dk3, US-MMS, and US-PFa, the reduced GPP at peak seasons is closer to measurements (not shown), leading to smaller biases for simulations. On average, the χ^2 decreases by 3-8% at these sites, depending on the O_3 sensitivity in the simulation (Table 3 and Fig. 3). Finally, the simulated annual GPP averaged over all

NACP sites changes from 3.8 g C m^{-2} day^{-1} to 3.6 g C m^{-2} day^{-1} with the high O_3 sensitivity simulation case, closer to the observations of 3.0 g C m^{-2} day^{-1}. The bias-correction from O_3 damage is much smaller relative to the effect of phenology (Fig. 3). Moreover, the O_3-induced damage does not improve the GPP correlation between observations and simulations, which remains similar at ~0.8 (for 40 sites) with and without O_3 effects (Fig. S5).

3.4 Evaluation of simulated O_3 vegetation damage against field and laboratory data

We compare the simulated O_3 damage effect with field and laboratory measurements from the published literature (Fig. 6). In total, 14 additional sensitivity experiments are performed with different levels of [O_3] at each NACP site (see section 2.2.1). GPP reductions increase accordingly with the increasing [O_3] (Fig. 6). For a given [O_3], the O_3 damage effect is strongest for C4 crops (despite the lower g_s:A_{net} ratio) but weakest for shrubland. YIBs simulates reasonable O_3 damage to GPP for all model PFTs compared to the meta-analyses of Wittig et al. (2007) and Lombardozzi et al. (2013). Field studies in shrubland are limited. Zhang et al. (2012) investigated the responses of four shrub species to [O_3]=70 ppbv and found large reductions in net photosynthesis of 50-60%. The average O_3-free A_{net} of those shrub species was 8-16 g [C] m^{-2} s^{-1}, much higher than even the gross photosynthesis (A) of 6 g [C] m^{-2} s^{-1} at the shrub NACP sites, likely because the latter are located in dry and/or cold areas (Fig. S1). The YIBs simulated O_3 vegetation damage effects for C4 plants are in good agreement with field measurements from Taylor et al. (2002) and Grantz et al. (2012). In the case of C3 grass and C3 crop, the model simulates consistent GPP reduction percentages with observations from Feng et al. (2008) for wheat, Foot et al. (1996) for colluna vulgaris, and Mulchi et al. (1992) for soybean. However, these O_3 damage results are all >50% less than for available measurements in rice crops (Ishii et al., 2004; Ainsworth et al., 2008), suggesting that rice may have much higher O_3 sensitivity than other C3 plants. In the U.S. rice plantation area is much smaller than that of soybean and corn. Therefore, we adopt the O_3 sensitivity parameters for C3/C4 plants shown in Table 1 for the regional simulations.

3.5 O_3 vegetation damage effect on GPP in U.S. region

High values of simulated summertime GPP (including O_3 damage effect) appear east of 95°W in the U.S. (Fig. 7a), because the land surface there is covered by crops and forests. A high center of GPP (> 10 g C m^{-2} day^{-1}) appears over cropland in the north central U.S. In the western U.S., the coverage of grass and shrub and the low water availability (low precipitation and soil moisture) over semi-arid regions lead to low carbon assimilation rate. The regional gridded simulated GPP reproduces the JJA growing season average NACP site-level fluxes with a correlation coefficient of 0.62 for 32 sites below 50°N (points in Fig. 7a). The correlation is lower than the 0.84 estimated for the site-level simulation METsite_LAImerra at the same sites and the same season. Since the meteorological forcings and LAI are similar, the difference in land cover, ISLSCP versus site definitions (Fig. S1 and Fig. S2), accounts for the discrepancy between regional and site-level simulations.

On average, the simulated summer GPP (including the high O_3 damage effect) is 9.5 g C m^{-2} day^{-1} in the eastern U.S. (east of 95°W) and 3.9 g C m^{-2} day^{-1} in the western U.S. (west of 95°W), giving a mean value of 6.1 g C m^{-2} day^{-1} for the U.S. region. The total carbon uptake is estimated to be 4.43 ± 0.18 Pg C during the summer growing season, accounting for 57-60% of the annual average value of 7.59 ± 0.25 Pg C over the 1998-2007 period. Our estimate of annual carbon uptake is consistent with previous published estimates. For example, Xiao et al. (2010) upscaled site-level GPP flux to continental scale with a regression tree approach based on both NACP fluxes and remote-sensing variables. They estimated that the total GPP in U.S. ranges from 6.91 to 7.33 Pg C per year during 2000-2006. Using the same observations but with a process-based biogeochemical model, Chen et al. (2011) estimated a range of 7.02-7.78 Pg C per year for 2000-2005, which is even closer to our estimate.

We calculate both O_3 stomatal flux (Fig. 7b) and the resultant damage on GPP (Fig. 8) in the U.S. region for the 1998-2007 period. High O_3 stomatal flux is predicted in the eastern U.S. due to co-location of the high GPP (medium to high stomatal conductance)

519 and the substantial ambient [O_3]. On average, the summertime O_3 plant uptake is 117
520 μmol m^{-2} day^{-1}, with 207 μmol m^{-2} day^{-1} in the eastern U.S. and 59 μmol m^{-2} day^{-1} in the
521 western U.S. Following the O_3 stomatal flux, the largest mean GPP reductions are
522 predicted for the eastern U.S. growing season, in the range 4-8% depending on the O_3
523 sensitivity applied in the simulations (Fig. 8). Locally, reduction fraction reaches as high
524 as 11-17% in areas with high [O_3] pollution, such as Michigan, Indiana, Ohio, and states
525 along the northeast coast. Despite high surface [O_3] over mountainous elevated areas in
526 the West (Fig. 4), impacts on GPP are limited due to the low stomatal conductance and
527 low photosynthetic rate there. The Pacific northwestern forests are an exception, with a
528 moderate GPP reduction of 1-7%. On average, the total summer GPP is reduced by 2-5%
529 due to O_3 damage effects in the U.S. Similar reduction fractions are predicted for the
530 annual GPP.
531
532 U.S. surface [O_3] exhibits a decreasing trend over the past 2 decades, especially in the
533 eastern U.S., due to precursor emission controls (Lefohn et al., 2010). However, the
534 community continues to debate how surface [O_3] will respond to future emissions and
535 climate change. On the one hand, surface [O_3] may decline by the mid 21st century due to
536 large reductions in regional anthropogenic precursor emissions (Wu et al., 2008). On the
537 other hand, climate change effects alone may increase local surface [O_3] due to the
538 warmer, drier, and more stable environment (Leibensperger et al., 2008; Wu et al., 2008).
539 Due to the uncertainty in future surface [O_3] projections, our strategy here is to perform
540 four additional sensitivity experiments with ±25% changes in [O_3] for each O_3 sensitivity
541 case. Increases of 25% in [O_3] may reduce GPP in the eastern U.S. by 6-11%, with a
542 maximum local reduction of 25% for the high O_3 sensitivity case (Fig. 9d). The damage
543 magnitude with low O_3 sensitivity (Fig. 9b) mimics the present-day estimate with high O_3
544 sensitivity (Fig. 8b). In contrast, the O_3 damage to the eastern U.S. GPP is as low as 2-4%
545 in response to 25% decreases in [O_3] (Figs. 9a, c), suggesting a substantial co-benefit to
546 ecosystem-health of O_3 precursor emissions control.
547
548 **4. Conclusions**
549

We have performed an updated assessment of O_3 vegetation damage effects on GPP in the U.S. for the 1998-2007 period using the YIBs vegetation model. The semi-mechanistic parameterization of O_3 inhibition on photosynthesis proposed by Sitch et al. (2007) has been implemented into this process-based vegetation model. The simulated O_3 damage effects are consistent with laboratory and field measurements reported in previously published studies. We evaluated the simulated O_3-free and O_3-damaged GPP with *in situ* measurements from 40 NACP sites. The O_3-free and O_3-damaged GPP simulations capture the seasonality and interannual variability of GPP at most sites. The model GPP biases are lowest at forest and cropland sites but highest at grassland sites. Model GPP is highly sensitive to choice of LAI forcing. Simulations that apply MERRA LAI generally perform better (show lower biases) than those with MODIS LAI. In response to the simulated ambient [O_3] of 30-50 ppbv, simulated GPP decreases by 1-14% at the NACP sites, depending on the O_3 sensitivity and PFT type. Maximum reductions of 5-14% occur in two forest sites, where both O_3-free GPP and ambient [O_3] are relatively high. Inclusion of the O_3 damage offers only a small improvement to the simulated annual average GPP at NACP sites (from 3.8 g C m^{-2} day^{-1} to 3.6 g C m^{-2} day^{-1}) such that the model still overestimates the observational average of 3.0 g C m^{-2} day^{-1}. The model GPP overestimate is most likely related to the use of generic PFT-specific photosynthesis parameters and the satellite prescribed LAI that may not represent the local site LAI. In this work, we assumed a coupled response between photosynthesis and stomatal conductance. Emerging research has found that the O_3 vegetation damage effects can actually result in a loss of plant stomatal control, and a consequent decoupling of the stomatal response from photosynthesis inhibition (Lombardozzi et al., 2012a, b). Treatment of this decoupled response in the YIBs model would lead to a higher level of O_3 flux entering leaves, thus causing stronger damage. Interestingly, this mechanism would provide a way to improve the simulated GPP overestimates. However, other studies have suggested that the O_3 damage to GPP may be offset by the benefits of co-located nitrogen deposition (Ollinger et al., 2002; Felzer et al., 2007), or even limited by carbon-nitrogen interactions (Kvalevag and Myhre, 2013).

Regional simulations for the U.S. yield a summertime GPP (with high sensitivity O_3 damage) of 6.1 g C m^{-2} day^{-1} (9.5 g C m^{-2} day^{-1} in the eastern U.S. and 3.9 g C m^{-2} day^{-1} in the western U.S.). The total carbon uptake was estimated to be 4.43 ± 0.18 Pg C for the summer, accounting for 57-60% of the annual value of 7.59 ± 0.25 Pg C over the 1998-2007 period. Carbon assimilation rate is suppressed by 4-8% on average in the summertime eastern U.S. with maximum local damage of 11-17% in states close to the Great Lakes and along the eastern coast. When [O_3] is decreased by 25%, O_3 damage to GPP is only 2-4% in the eastern U.S., indicating substantial improvements to vegetation health and carbon assimilation rate. Previously, Felzer et al. (2004) found annual average O_3-induced NPP reductions of 3-7% over the U.S. for 1989-1993 and simulated the largest reductions in states close to the Great Lakes and along the East Coast, where the high O_3 sensitivity of crops makes the dominant contribution. Our study examined O_3 damage effects a decade later than Felzer et al. (2004) but gives consistent results. Qualitatively, this consistency between decades may be explained by the offsetting influences of (i) surface O_3 reductions due to air quality control legislation and (ii) GPP increases due to CO_2-fertilization and rising temperatures. Felzer et al. (2004) estimated a maximum local NPP reduction of 34%, which is double the maximum of 17% in our analyses. Furthermore, Felzer et al. (2004) found widespread reductions of > 6% in the Midwest where there is almost no O_3 impact in this study (Fig. 8). Differences between the studies are mostly likely driven by the use of different vegetation cover and LAI datasets, and the use of a semi-mechanistic flux-based uptake in this study versus the concentration-based uptake method elsewhere.

The current work has used an off-line approach. Yet, the O_3-vegetation-meteorology system is strongly coupled. For instance, plant productivity itself controls the emission of isoprene, a major O_3 precursor. The O_3-induced modification to stomatal conductance may inhibit evapotranspiration, leading to changes in canopy temperature, precipitation, soil moisture, and other surface hydrology and meteorology (Bernacchi et al., 2007; vanLoocke et al., 2012). In future work, we will study O_3 vegetation damage effects using YIBs embedded within a fully coupled global chemistry-climate model framework in order to account for these feedbacks including altered canopy energy fluxes and

611 partitioning between latent and sensible heat that drive regional climate and hydrology. In
612 addition, the O_3 damage algorithm parameters were calibrated using limited
613 measurements for a few plant species, and were based on biomass yield not
614 photosynthetic rate (Sitch et al., 2007). Future work will exploit recent extensive meta-
615 data analyses (Lombardozzi et al., 2013; Wittig et al., 2007) to refine the ozone damage
616 parameterization in YIBs including the decoupled modification of photosynthesis and
617 stomatal conductance.
618

619 **Acknowledgements**

620 The authors are grateful to B. Felzer and an anonymous reviewer for assistance in
621 evaluating this paper. Data for this analysis was provided by the North American Carbon
622 Program Site Synthesis. Funding for this research was provided by Yale University. This
623 project was supported in part by the facilities and staff of the Yale University Faculty of
624 Arts and Sciences High Performance Computing Center.

625

626 **References**

627 Ainsworth, E. A.: Rice production in a changing climate: a meta-analysis of responses to
628 elevated carbon dioxide and elevated ozone concentration, Global Change Biol., 14,
629 1642-1650, doi:10.1111/J.1365-2486.2008.01594.X, 2008.
630 Ainsworth, E. A., Yendrek, C. R., Sitch, S., Collins, W. J., and Emberson, L. D.: The
631 Effects of Tropospheric Ozone on Net Primary Productivity and Implications for
632 Climate Change, Annu. Rev. Plant Biol., 63, 637-661, doi:10.1146/Annurev-Arplant-
633 042110-103829, 2012.
634 Barr, A., Ricciuto, D., Schaefer, K., Richardson, A., Agarwal, D., Thornton, P., Davis,
635 K., Jackson, B., Cook, R., Hollinger, D., Ingen, C. v., Amiro, B., Andrews, A., Arain,
636 M., Baldocchi, D., Black, T., Bolstad, P., Curtis, P., Desai, A., Dragoni, D., Flanagan,
637 L., Gu, L., Katul, G., Law, B., Lafleur, P., Margolis, H., Matamala, R., Meyers, T.,
638 McCaughey, H., Monson, R., Munger, J., Oechel, W., Oren, R., Roulet, N., Torn, M.,
639 and Verma, S.: NACP Site: Tower Meteorology, Flux Observations with Uncertainty,
640 and Ancillary Data, Oak Ridge National Laboratory Distributed Active Archive
641 Center, Oak Ridge, Tennessee, USA, 2013.
642 Bell, N., Koch, D., and Shindell, D. T.: Impacts of chemistry-aerosol coupling on
643 tropospheric ozone and sulfate simulations in a general circulation model, J. Geophys.
644 Res., 110, D14305, doi:10.1029/2004jd005538, 2005.
645 Bernacchi, C. J., Kimball, B. A., Quarles, D. R., Long, S. P., and Ort, D. R.: Decreases in
646 stomatal conductance of soybean under open-air elevation of [CO(2)] are closely
647 coupled with decreases in ecosystem evapotranspiration, Plant Physiol., 143, 134-144,
648 doi:10.1104/Pp.106.089557, 2007.
649 Bloomer, B. J., Vinnikov, K. Y., and Dickerson, R. R.: Changes in seasonal and diurnal
650 cycles of ozone and temperature in the eastern US, Atmos. Environ., 44, 2543-2551,
651 doi:10.1016/J.Atmosenv.2010.04.031, 2010.
652 Bonan, G. B., Lawrence, P. J., Oleson, K. W., Levis, S., Jung, M., Reichstein, M.,
653 Lawrence, D. M., and Swenson, S. C.: Improving canopy processes in the Community
654 Land Model version 4 (CLM4) using global flux fields empirically inferred from
655 FLUXNET data, J. Geophys. Res., 116, G02014, doi:10.1029/2010jg001593, 2011.

656 Chen, M., Zhuang, Q., Cook, D. R., Coulter, R., Pekour, M., Scott, R. L., Munger, J. W.,
657 and Bible, K.: Quantification of terrestrial ecosystem carbon dynamics in the
658 conterminous United States combining a process-based biogeochemical model and
659 MODIS and AmeriFlux data, Biogeosciences, 8, 2665-2688, doi:10.5194/Bg-8-2665-
660 2011, 2011.
661 Chiariello, N. R.: Phenology of California grasslands, in: Grassland structure and
662 function: California annual grassland, edited by: Huenneke, L. F., and Mooney, H. A.,
663 Kluwer Academic Publishers, Dordrecht, 47-58, 1989.
664 Collatz, G. J., Ball, J. T., Grivet, C., and Berry, J. A.: Physiological and Environmental-
665 Regulation of Stomatal Conductance, Photosynthesis and Transpiration - a Model That
666 Includes a Laminar Boundary-Layer, Agr. Forest Meteorol., 54, 107-136,
667 doi:10.1016/0168-1923(91)90002-8, 1991.
668 Cooper, O. R., Parrish, D. D., Stohl, A., Trainer, M., Nedelec, P., Thouret, V., Cammas,
669 J. P., Oltmans, S. J., Johnson, B. J., Tarasick, D., Leblanc, T., McDermid, I. S., Jaffe,
670 D., Gao, R., Stith, J., Ryerson, T., Aikin, K., Campos, T., Weinheimer, A., and Avery,
671 M. A.: Increasing springtime ozone mixing ratios in the free troposphere over western
672 North America, Nature, 463, 344-348, doi:10.1038/Nature08708, 2010.
673 Desai, A. R., Noormets, A., Bolstad, P. V., Chen, J. Q., Cook, B. D., Davis, K. J.,
674 Euskirchen, E. S., Gough, C. M., Martin, J. G., Ricciuto, D. M., Schmid, H. P., Tang,
675 J. W., and Wang, W. G.: Influence of vegetation and seasonal forcing on carbon
676 dioxide fluxes across the Upper Midwest, USA: Implications for regional scaling, Agr.
677 Forest Meteorol., 148, 288-308, doi:10.1016/J.Agrformet.2007.08.001, 2008.
678 Farquhar, G. D., Caemmerer, S. V., and Berry, J. A.: A Biochemical-Model of
679 Photosynthetic Co2 Assimilation in Leaves of C-3 Species, Planta, 149, 78-90,
680 doi:10.1007/Bf00386231, 1980.
681 Felzer, B. S., Cronin, T., Reilly, J. M., Melilloa, J. M., and Wang, X. D.: Impacts of
682 ozone on trees and crops, Comptes rendus Geoscience, 339, 784-798,
683 doi:10.1016/J.Crte.2007.08.008, 2007.
684 Felzer, B., Kicklighter, D., Melillo, J., Wang, C., Zhuang, Q., and Prinn, R.: Effects of
685 ozone on net primary production and carbon sequestration in the conterminous United

States using a biogeochemistry model, Tellus B, 56, 230-248, doi:10.1111/J.1600-0889.2004.00097.X, 2004.

Felzer, B., Reilly, J., Melillo, J., Kicklighter, D., Sarofim, M., Wang, C., Prinn, R., and Zhuang, Q.: Future effects of ozone on carbon sequestration and climate change policy using a global biogeochemical model, Climatic Change, 73, 345-373, doi:10.1007/S10584-005-6776-4, 2005.

Feng, Z. Z., Kobayashi, K., and Ainsworth, E. A.: Impact of elevated ozone concentration on growth, physiology, and yield of wheat (Triticum aestivum L.): a meta-analysis, Global Change Biol., 14, 2696-2708, doi:10.1111/J.1365-2486.2008.01673.X, 2008.

Foot, J. P., Caporn, S. J. M., Lee, J. A., and Ashenden, T. W.: The effect of long-term ozone fumigation on the growth, physiology and frost sensitivity of Calluna vulgaris, New Phytol., 133, 503-511, doi:10.1111/J.1469-8137.1996.Tb01918.X, 1996.

Friend, A. D., and Kiang, N. Y.: Land surface model development for the GISS GCM: Effects of improved canopy physiology on simulated climate, J Climate, 18, 2883-2902, doi:10.1175/Jcli3425.1, 2005.

Goodale, C. L., Apps, M. J., Birdsey, R. A., Field, C. B., Heath, L. S., Houghton, R. A., Jenkins, J. C., Kohlmaier, G. H., Kurz, W., Liu, S. R., Nabuurs, G. J., Nilsson, S., and Shvidenko, A. Z.: Forest carbon sinks in the Northern Hemisphere, Ecol. Appl., 12, 891-899, Doi 10.2307/3060997, 2002.

Grantz, D. A., Vu, H. B., Tew, T. L., and Veremis, J. C.: Sensitivity of Gas Exchange Parameters to Ozone in Diverse C-4 Sugarcane Hybrids, Crop Sci., 52, 1270-1280, doi:10.2135/Cropsci2011.08.0413, 2012.

Gregg, J. W., Jones, C. G., and Dawson, T. E.: Urbanization effects on tree growth in the vicinity of New York City, Nature, 424, 183-187, doi:10.1038/Nature01728, 2003.

Hall, F. G., de Colstoun, E. B., Collatz, G. J., Landis, D., Dirmeyer, P., Betts, A., Huffman, G. J., Bounoua, L., and Meeson, B.: ISLSCP Initiative II global data sets: Surface boundary conditions and atmospheric forcings for land-atmosphere studies, J. Geophys. Res., 111, D22s01, doi:10.1029/2006jd007366, 2006.

Heagle, A. S., Kress, L. W., Temple, P. J., Kohut, R. J., Miller, J. E., and Heggestad, H. E.: Factors influencing ozone dose-yield response relationships in open-top chamber

717 studies, in: Assessment of crop loss from air pollutants, edited by: Heck, W. W.,
718 Taylor, O. C., and Tingey, D. T., Elsevier Applied Science, New York, 141-179, 1989.
719 Henebry, G. M.: Grasslands of the North American Great Plains, in: Phenology: an
720 integrative environmental science, edited by: Schwartz, M. D., Kluwer Academic
721 Publishers, Dordrecht, 157-174, 2003.
722 Hollaway, M. J., Arnold, S. R., Challinor, A. J., and Emberson, L. D.: Intercontinental
723 trans-boundary contributions to ozone-induced crop yield losses in the Northern
724 Hemisphere, Biogeosciences, 9, 271-292, doi:10.5194/Bg-9-271-2012, 2012.
725 Huntingford, C., Cox, P. M., Mercado, L. M., Sitch, S., Bellouin, N., Boucher, O., and
726 Gedney, N.: Highly contrasting effects of different climate forcing agents on terrestrial
727 ecosystem services, Philos. T. R. Soc. A, 369, 2026-2037,
728 doi:10.1098/Rsta.2010.0314, 2011.
729 Huntzinger, D. N., Post, W. M., Wei, Y., Michalak, A. M., West, T. O., Jacobson, A. R.,
730 Baker, I. T., Chen, J. M., Davis, K. J., Hayes, D. J., Hoffman, F. M., Jain, A. K., Liu,
731 S., McGuire, A. D., Neilson, R. P., Potter, C., Poulter, B., Price, D., Raczka, B. M.,
732 Tian, H. Q., Thornton, P., Tomelleri, E., Viovy, N., Xiao, J., Yuan, W., Zeng, N.,
733 Zhao, M., and Cook, R.: North American Carbon Program (NACP) regional interim
734 synthesis: Terrestrial biospheric model intercomparison, Ecol. Model, 232, 144-157,
735 doi: 10.1016/J.Ecolmodel.2012.02.004, 2012.
736 Ishii, S., Marshall, F. M., and Bell, J. N. B.: Physiological and morphological responses
737 of locally grown Malaysian rice cultivars (Oryza sativa L.) to different ozone
738 concentrations, Water Air Soil Poll., 155, 205-221,
739 doi:10.1023/B:Wate.0000026528.86641.5b, 2004.
740 Jaffe, D., and Ray, J.: Increase in surface ozone at rural sites in the western US, Atmos.
741 Environ., 41, 5452-5463, doi:10.1016/J.Atmosenv.2007.02.34, 2007.
742 Karnosky, D. F., Skelly, J. M., Percy, K. E., and Chappelka, A. H.: Perspectives
743 regarding 50 years of research on effects of tropospheric ozone air pollution on US
744 forests, Environ. Pollut., 147, 489-506, doi:10.1016/J.Envpol.2006.08.043, 2007.
745 Kvalevag, M. M., and Myhre, G.: The effect of carbon-nitrogen coupling on the reduced
746 land carbon sink caused by tropospheric ozone, Geophys Res. Lett., 40, 3227-3231,
747 doi:10.1002/Grl.50572, 2013.

King, A. W., Hayes, D. J., Huntzinger, D. N., West, T. O., and Post, W. M.: North American carbon dioxide sources and sinks: magnitude, attribution, and uncertainty, Front. Ecol. Environ., 10, 512-519, doi: 10.1890/120066, 2012.

Knyazikhin, Y., Martonchik, J. V., Myneni, R. B., Diner, D. J., and Running, S. W.: Synergistic algorithm for estimating vegetation canopy leaf area index and fraction of absorbed photosynthetically active radiation from MODIS and MISR data, J. Geophys. Res., 103, 32257-32275, doi:10.1029/98jd02462, 1998.

Lefohn, A. S., Shadwick, D., and Oltmans, S. J.: Characterizing changes in surface ozone levels in metropolitan and rural areas in the United States for 1980-2008 and 1994-2008, Atmos. Environ., 44, 5199-5210, doi:10.1016/J.Atmosenv.2010.08.049, 2010.

Leibensperger, E. M., Mickley, L. J., and Jacob, D. J.: Sensitivity of US air quality to mid-latitude cyclone frequency and implications of 1980-2006 climate change, Atmos. Chem. Phys., 8, 7075-7086, 2008.

Lombardozzi, D., Levis, S., Bonan, G., and Sparks, J. P.: Predicting photosynthesis and transpiration responses to ozone: decoupling modeled photosynthesis and stomatal conductance, Biogeosciences, 9, 3113-3130, doi:10.5194/bg-9-3113-2012, 2012a.

Lombardozzi, D., Sparks, J. P., Bonan, G., and Levis, S.: Ozone exposure causes a decoupling of conductance and photosynthesis: implications for the Ball-Berry stomatal conductance model, Oecologia, 169, 651-659, doi:10.1007/S00442-011-2242-3, 2012b.

Lombardozzi, D., Sparks, J. P., and Bonan, G.: Integrating O3 influences on terrestrial processes: photosynthetic and stomatal response data available for regional and global modeling, Biogeosciences, 10, 6815-6831, 10.5194/bg-10-6815-2013, 2013.

Mulchi, C. L., Slaughter, L., Saleem, M., Lee, E. H., Pausch, R., and Rowland, R.: Growth and Physiological-Characteristics of Soybean in Open-Top Chambers in Response to Ozone and Increased Atmospheric Co2, Agr Ecosyst Environ, 38, 107-118, doi:10.1016/0167-8809(92)90172-8, 1992.

Oleson, K. W., Lawrence, D. M., Bonan, G. B., Flanne, M. G., Kluzek, E., Lawrence, P. J., Levis, S., Swenson, S. C., and Thornton, P. E.: Technical Description of version 4.0 of the Community Land Model (CLM), National Center for Atmospheric Research, Boulder, CONCAR/TN-478+STR, 2010.

779 Ollinger, S. V., Aber, J. D., Reich, P. B., and Freuder, R. J.: Interactive effects of
780 nitrogen deposition, tropospheric ozone, elevated CO2 and land use history on the
781 carbon dynamics of northern hardwood forests, Global Change Biol., 8, 545-562,
782 doi:10.1046/J.1365-2486.2002.00482.X, 2002.
783 Pacala, S. W., Hurtt, G. C., Baker, D., Peylin, P., Houghton, R. A., Birdsey, R. A., Heath,
784 L., Sundquist, E. T., Stallard, R. F., Ciais, P., Moorcroft, P., Caspersen, J. P.,
785 Shevliakova, E., Moore, B., Kohlmaier, G., Holland, E., Gloor, M., Harmon, M. E.,
786 Fan, S. M., Sarmiento, J. L., Goodale, C. L., Schimel, D., and Field, C. B.: Consistent
787 land- and atmosphere-based US carbon sink estimates, Science, 292, 2316-2320,
788 doi:10.1126/Science.1057320, 2001.
789 Pan, Y. D., Birdsey, R. A., Fang, J. Y., Houghton, R., Kauppi, P. E., Kurz, W. A.,
790 Phillips, O. L., Shvidenko, A., Lewis, S. L., Canadell, J. G., Ciais, P., Jackson, R. B.,
791 Pacala, S. W., McGuire, A. D., Piao, S. L., Rautiainen, A., Sitch, S., and Hayes, D.: A
792 Large and Persistent Carbon Sink in the World's Forests, Science, 333, 988-993,
793 doi:10.1126/Science.1201609, 2011.
794 Puma, M. J., Koster, R. D., and Cook, B. I.: Phenological versus meteorological controls
795 on land-atmosphere water and carbon fluxes, J. Geophys. Res., 118, 14-29,
796 doi:10.1029/2012jg002088, 2013.
797 Reichle, R. H., Koster, R. D., De Lannoy, G. J. M., Forman, B. A., Liu, Q., Mahanama,
798 S. P. P., and Toure, A.: Assessment and Enhancement of MERRA Land Surface
799 Hydrology Estimates, J Climate, 24, 6322-6338, doi:10.1175/Jcli-D-10-05033.1, 2011.
800 Ricciuto, D., Schaefer, K., Thornton, P., Davis, K., Cook, R., Liu, S., Anderson, R.,
801 Arain, M., Baker, I., Chen, J., Dietze, M., Grant, R., Izaurralde, C., Jain, A., King, A.,
802 Kucharik, C., Liu, S., Lokupitiya, E., Luo, Y., Peng, C., Poulter, B., Price, D., Riley,
803 W., Sahoo, A., Tian, H., Tonitto, C., and Verbeeck, H.: NACP Site: Terrestrial
804 Biosphere Model and Aggregated Flux Data in Standard Format, Oak Ridge National
805 Laboratory Distributed Active Archive Center, Oak Ridge, Tennessee, USA, 2013.
806 Rienecker, M. M., Suarez, M. J., Gelaro, R., Todling, R., Bacmeister, J., Liu, E.,
807 Bosilovich, M. G., Schubert, S. D., Takacs, L., Kim, G. K., Bloom, S., Chen, J. Y.,
808 Collins, D., Conaty, A., Da Silva, A., Gu, W., Joiner, J., Koster, R. D., Lucchesi, R.,
809 Molod, A., Owens, T., Pawson, S., Pegion, P., Redder, C. R., Reichle, R., Robertson,

F. R., Ruddick, A. G., Sienkiewicz, M., and Woollen, J.: MERRA: NASA's Modern-Era Retrospective Analysis for Research and Applications, J Climate, 24, 3624-3648, doi:10.1175/Jcli-D-11-00015.1, 2011.

Rigby, M., Prinn, R. G., Fraser, P. J., Simmonds, P. G., Langenfelds, R. L., Huang, J., Cunnold, D. M., Steele, L. P., Krummel, P. B., Weiss, R. F., O'Doherty, S., Salameh, P. K., Wang, H. J., Harth, C. M., Muhle, J., and Porter, L. W.: Renewed growth of atmospheric methane, Geophys. Res. Lett., 35, L22805, doi:10.1029/2008gl036037, 2008.

Rudorff, B. F. T., Mulchi, C. L., Lee, E. H., Rowland, R., and Pausch, R.: Effects of enhanced O-3 and CO2 enrichment on plant characteristics in wheat and corn, Environ. Pollut., 94, 53-60, doi:10.1016/S0269-7491(96)00050-4, 1996.

Schaefer, K., Schwalm, C. R., Williams, C., Arain, M. A., Barr, A., Chen, J. M., Davis, K. J., Dimitrov, D., Hilton, T. W., Hollinger, D. Y., Humphreys, E., Poulter, B., Raczka, B. M., Richardson, A. D., Sahoo, A., Thornton, P., Vargas, R., Verbeeck, H., Anderson, R., Baker, I., Black, T. A., Bolstad, P., Chen, J. Q., Curtis, P. S., Desai, A. R., Dietze, M., Dragoni, D., Gough, C., Grant, R. F., Gu, L. H., Jain, A., Kucharik, C., Law, B., Liu, S. G., Lokipitiya, E., Margolis, H. A., Matamala, R., McCaughey, J. H., Monson, R., Munger, J. W., Oechel, W., Peng, C. H., Price, D. T., Ricciuto, D., Riley, W. J., Roulet, N., Tian, H. Q., Tonitto, C., Torn, M., Weng, E. S., and Zhou, X. L.: A model-data comparison of gross primary productivity: Results from the North American Carbon Program site synthesis, J. Geophys. Res., 117, G03010, doi:10.1029/2012jg001960, 2012.

Shindell, D. T., Faluvegi, G., Unger, N., Aguilar, E., Schmidt, G. A., Koch, D. M., Bauer, S. E., and Miller, R. L.: Simulations of preindustrial, present-day, and 2100 conditions in the NASA GISS composition and climate model G-PUCCINI, Atmos. Chem. Phys., 6, 4427-4459, 2006.

Shindell, D. T., Pechony, O., Voulgarakis, A., Faluvegi, G., Nazarenko, L., Lamarque, J. F., Bowman, K., Milly, G., Kovari, B., Ruedy, R., and Schmidt, G. A.: Interactive ozone and methane chemistry in GISS-E2 historical and future climate simulations, Atmos. Chem. Phys., 13, 2653-2689, doi:10.5194/Acp-13-2653-2013, 2013.

840 Sitch, S., Cox, P. M., Collins, W. J., and Huntingford, C.: Indirect radiative forcing of
841 climate change through ozone effects on the land-carbon sink, Nature, 448, 791-794,
842 doi:10.1038/Nature06059, 2007.
843 Spitters, C. J. T., Toussaint, H. A. J. M., and Goudriaan, J.: Separating the Diffuse and
844 Direct Component of Global Radiation and Its Implications for Modeling Canopy
845 Photosynthesis .1. Components of Incoming Radiation, Agr. Forest Meteorol., 38,
846 217-229, doi:10.1016/0168-1923(86)90060-2, 1986.
847 Taylor, M. D., Sinn, J. P., Davis, D. D., and Pell, E. J.: The impact of ozone on a salt
848 marsh cordgrass (Spartina alterniflora), Environ. Pollut., 120, 701-705, 2002.
849 Unger, N.: Global climate impact of civil aviation for standard and desulfurized jet fuel,
850 Geophys. Res. Lett., 38, L20803, doi:10.1029/2011gl049289, 2011.
851 Unger, N., and Pan, J. L.: New Directions: Enduring ozone, Atmos. Environ., 55, 456-
852 458, doi:10.1016/J.Atmosenv.2012.03.036, 2012.
853 Unger, N., Harper, K., Zheng, Y., Kiang, N. Y., Aleinov, I., Arneth, A., Schurgers, G.,
854 Amelynck, C., Goldstein, A., Guenther, A., Heinesch, B., Hewitt, C. N., Karl, T.,
855 Laffineur, Q., Langford, B., McKinney, K. A., Misztal, P., Potosnak, M., Rinne, J.,
856 Pressley, S., Schoon, N., and Serça, D.: Photosynthesis-dependent isoprene emission
857 from leaf to planet in a global carbon–chemistry–climate model, Atmos. Chem. Phys.,
858 13, 10243-10269, doi:10.5194/acp-13-10243-2013, 2013.
859 von Caemmerer, S., and Farquhar, G. D.: Some Relationships between the Biochemistry
860 of Photosynthesis and the Gas-Exchange of Leaves, Planta, 153, 376-387, 1981.
861 VanLoocke, A., Betzelberger, A. M., Ainsworth, E. A., and Bernacchi, C. J.: Rising
862 ozone concentrations decrease soybean evapotranspiration and water use efficiency
863 whilst increasing canopy temperature, New Phytol., 195, 164-171, doi:10.1111/J.1469-
864 8137.2012.04152.X, 2012.
865 Wittig, V. E., Ainsworth, E. A., and Long, S. P.: To what extent do current and projected
866 increases in surface ozone affect photosynthesis and stomatal conductance of trees? A
867 meta-analytic review of the last 3 decades of experiments, Plant Cell Environ., 30,
868 1150-1162, doi:10.1111/J.1365-3040.2007.01717.X, 2007.

869 Wu, S. L., Mickley, L. J., Leibensperger, E. M., Jacob, D. J., Rind, D., and Streets, D. G.:
870 Effects of 2000-2050 global change on ozone air quality in the United States, J.
871 Geophys. Res., 113, D06302, doi:10.1029/2007jd008917, 2008.
872 Xiao, J. F., Zhuang, Q. L., Law, B. E., Chen, J. Q., Baldocchi, D. D., Cook, D. R., Oren,
873 R., Richardson, A. D., Wharton, S., Ma, S. Y., Martin, T. A., Verma, S. B., Suyker, A.
874 E., Scott, R. L., Monson, R. K., Litvak, M., Hollinger, D. Y., Sun, G., Davis, K. J.,
875 Bolstad, P. V., Burns, S. P., Curtis, P. S., Drake, B. G., Falk, M., Fischer, M. L.,
876 Foster, D. R., Gu, L. H., Hadley, J. L., Katul, G. G., Roser, Y., McNulty, S., Meyers,
877 T. P., Munger, J. W., Noormets, A., Oechel, W. C., Paw, K. T., Schmid, H. P., Starr,
878 G., Torn, M. S., and Wofsy, S. C.: A continuous measure of gross primary production
879 for the conterminous United States derived from MODIS and AmeriFlux data, Remote
880 Sens. Environ., 114, 576-591, doi:10.1016/J.Rse.2009.10.013, 2010.
881 Zhang, L., Su, B. Y., Xu, H., and Li, Y. G.: Growth and photosynthetic responses of four
882 landscape shrub species to elevated ozone, Photosynthetica, 50, 67-76,
883 doi:10.1007/S11099-012-0004-Z, 2012.
884
885

Table 1. Parameters for vegetation model and O_3 damage scheme

PFT [a]	TDA	GRAC3	GRAC4	SHR	DBF	ENF	TRF	CRO	
Carboxylation	C3	C3	C4	C3	C3	C3	C3	C3 [b]	C4 [b]
$V_{max\,25}$ (μmol m^{-2} s^{-1})	33	43	24	25	30	43	75	40	40
m	9	11	5	9	9	9	9	11	5
b (mmol m^{-2} s^{-1})	2	8	2	2	2	2	2	8	2
O3T (nmol m^{-2} s^{-1})	1.6	5	5	1.6	1.6	1.6	1.6	5	5
a (high) ($mmol^{-1}$ m^{-2})	0.1	1.4	0.735	0.1	0.15	0.075	0.15	1.4	0.735
a (low) ($mmol^{-1}$ m^{-2})	0.03	0.25	0.13	0.03	0.04	0.02	0.04	0.25	0.13

[a] Plant function types (PFTs) are tundra (TDA), C3 grassland (GRAC3), C4 savanna/grassland (GRAC4), shrubland (SHR), deciduous broadleaf forest (DBF), evergreen needleleaf forest (ENF), tropical rainforest (TRF), and cropland (CRO).

[b] For site-level simulations, we consider CRO as C4 plant. For regional simulation, we consider half CRO as C3 plants (soybean) and the rest C4 plant (corn).

Table 2. Description of the site-level simulations.

ID	Simulations [a]	Meteorology		Vegetation (LAI)		Incl. O_3 [c]
		Site	MERRA	MODIS	MERRA	
1	METmerra_LAImodis		Yes	Yes		
2	METsite_LAImodis [b]	Yes	Yes	Yes		
3	METmerra_LAImerra		Yes		Yes	
4	METsite_LAImerra [b]	Yes	Yes		Yes	
5	METsite_LAImerra_LO3 [b]	Yes	Yes		Yes	Low [d]
6	METsite_LAImerra_HO3 [b]	Yes	Yes		Yes	High [d]

[a] The name of each simulation is composed of at least two words. The prefix indicates the source of meteorological forcings. The suffix or the second word indicates the sources of vegetation forcings.

[b] For simulations with prefix 'SITE' use site-based meteorological forcings, which are gap-filled with MERRA-land reanalyses.

[c] Ambient [O_3] is applied at each site.

[d] Low and high indicate the sensitivity of GPP to [O_3] defined by the coefficient *a* in Table 1.

Table 3. Statistics [a] for site-level simulations.

		R^2			RMSE			χ^2		
ID	Simulations	min	max	mean	min	max	mean	min	max	total
1	METmerra_LAImodis	0.14	0.85	0.63	1.2	6.4	3.0	1.4	37.6	9.4
2	METsite_LAImodis	0.16	0.85	0.67	1.1	5.8	2.9	1.1	39.6	8.9
3	METmerra_LAImerra	0	0.88	0.66	1.3	4.2	2.4	1.2	16.6	4.8
4	METsite_LAImerra	0	0.87	0.68	1.0	4.2	2.3	1.2	13.4	4.1
5	METsite_LAImerra_LO3	0	0.88	0.69	1.0	4.1	2.3	1.1	13.0	3.9
6	METsite_LAImerra_HO3	0	0.88	0.69	1.0	4.1	2.2	1.0	12.3	3.7

[a] Statistics include minimum and maximum values of R^2, RMSE, and χ^2 for 35 NCAP sites with $\chi^2 < 16$ (Fig. S6a). We also calculate the mean values of R^2 and RMSE for these sites. We calculate the total χ^2 (shown as red bars in Fig. 3) using all the available observations over all sites.

Appendix

Table A. Descriptions of NACP sites in Canada (CA-) and U.S. (US-) [a]

Site	PFT [b]	Description	Longitude	Latitude	Period
CA-Ca1	ENF	Campbell River	125.3°W	49.9°N	1998-2006
CA-Ca2	ENF	Campbell River	125.3°W	49.9°N	2001-2006
CA-Ca3	ENF	Campbell River	124.9°W	49.5°N	2002-2006
CA-Gro	MF	Groundhog River	82.2°W	48.2°N	2004-2006
CA-Let	GRA	Lethbridge Grassland	112.9°W	49.7°N	2001-2007
CA-Mer	WET	Eastern Peatland	75.5°W	45.4°N	1999-2006
CA-NS1	ENF	UCI Chronosequence	124.9°W	49.5°N	2001-2005
CA-Oas	DBF	BERMS	106.2°W	53.6°N	1997-2006
CA-Obs	ENF	BERMS	105.1°W	54.0°N	2000-2006
CA-Ojp	ENF	BERMS	104.7°W	53.9°N	2000-2006
CA-Qfo	ENF	Quebec	74.3°W	49.7°N	2004-2006
CA-SJ1	ENF	BERMS	104.7°W	53.9°N	2002-2005
CA-SJ2	ENF	BERMS	104.6°W	53.9°N	2004-2006
CA-SJ3	ENF	BERMS	104.6°W	53.9°N	2005-2006
CA-TP4	ENF	Turkey Point	80.4°W	42.7°N	2003-2007
CA-WP1	WET	Western Peatland	112.5°W	55.0°N	2004-2007
US-ARM	GRA [c]	Southern Great Plains	97.5°W	36.6°N	2003-2007
US-Dk3	ENF	Duke Forest	79.1°W	36.0°N	1998-2005
US-Ha1	DBF	Harvard Forest	72.2°W	42.5°N	1992-2006
US-Ho1	ENF	Howland Forest	68.7°W	45.2°N	1996-2004
US-IB1	CRO	Fermi Lab	88.2°W	41.9°N	2006
US-IB2	GRA	Fermi	88.2°W	41.8°N	2005-2006
US-Los	WET	Lost Creek	90.0°W	46.1°N	2001-2006
US-MMS	DBF	Morgan Monroe State Forest	86.4°W	39.3°N	1999-2006
US-MOz	DBF	Missouri Ozark	92.2°W	38.7°N	2005-2007
US-Me2	ENF	Metolius	121.6°W	44.5°N	2002-2007
US-Me3	ENF	Metolius	121.6°W	44.3°N	2004-2005
US-Me5	ENF	Metolius	121.6°W	44.4°N	2000-2002
US-NR1	ENF	Niwot Ridge	105.5°W	40.0°N	1999-2007
US-Ne1	CRO	Mead	96.5°W	41.2°N	2002-2005
US-Ne2	CRO	Mead	96.5°W	41.2°N	2003-2005
US-Ne3	CRO	Mead	96.4°W	41.2°N	2002-2005
US-Pfa	MF	Park Falls	90.3°W	45.9°N	1997-2004
US-SO2	CSH	Sky Oaks	116.6°W	33.4°N	1999-2006
US-Shd	GRA	Shidler	96.7°W	36.9°N	1998-1999
US-Syv	MF	Sylvania Wilderness Area	89.3°W	46.2°N	2002-2006
US-Ton	WSA	Tonzi Ranch	121.0°W	38.4°N	2002-2007
US-UMB	DBF	UMBS	84.7°W	45.6°N	1999-2006
US-Var	GRA	Varia Ranch	121.0°W	38.4°N	2001-2007
US-WCr	DBF	Willow Creek	90.1°W	45.8°N	1999-2006

[a] Site information is adopted from Schaefer et al. (2012), except that the operational time span listed here is only for the period when measurements of GPP are available.

[b] PFT names are: evergreen needleleaf forest (ENF), deciduous broadleaf forest (DBF), grasslands (GRA), croplands (CRO), closed shrublands (CSH), mixed forests (MF), permanent wetlands (WET), and woody savannas (WSA).

940 [c] The land type at US-ARM is cropland in Schaefer et al. (2012). However, the site is
941 covered by cattle pasture and wheat fields (https://www.arm.gov/sites/sgp), which are
942 more like C3 grassland.
943
944
945

946 **Figure Captions**

947 **Fig. 1.** Comparison between monthly average GPP in the YIBs simulations and NACP
948 observations grouped by PFT type (where *in situ* measurements are available). The red
949 lines indicate linear regression between observations and simulation results. The
950 regression fits and correlation coefficients are shown on each panel. The land types
951 include evergreen needleleaf forest (ENF), deciduous broadleaf forest (DBF), shrublands
952 (SHR), grasslands (GRA), and croplands (CRO). The model-observation comparison for
953 each site is shown in Fig. S4.

954

955 **Fig. 2.** Histogram of (a) χ^2 for O_3-free GPP and changes in χ^2 after the inclusion of O_3
956 damage impact with (b) low and (c) high O_3 sensitivity. Each bar represents the number
957 of sites where the χ^2 or $\Delta\chi^2$ of simulations fall between the specific thresholds as defined
958 by the x-axis intervals. The minimum and maximum of χ^2 or $\Delta\chi^2$ are indicated as the two
959 ends of x-axis in the plots. The land cover definitions are: ENF, Evergreen Needleleaf
960 Forest; DBF, Deciduous Broadleaf Forest; SHR, Shrubland; GRA, Grasslands; CRO,
961 Croplands. Results for each site are detailed in Fig. S6.

962

963 **Fig. 3.** The calculated average χ^2 of GPP over NACP sites for 6 different simulations as
964 listed in Table 2. The blue bars are results for all 40 NACP sites. The red bars are results
965 excluding sites CA-Let, CA-NS1, US-Var, CA-SJ1, and CA-SJ2, where the simulated
966 site-level χ^2 is larger than 16 as shown in Fig. S6a.

967

968 **Fig. 4.** Validation of simulated June-July-August (JJA) summertime average surface (a,
969 b) diurnal mean and (c, d) daily maximum 8-hour average O_3 with *in situ* measurements
970 from (a, b) the EPA Clean Air Status and Trends Network (CASTNET) and (c, d) the
971 AIRDATA. For (b) and (d), the blue points indicate sites east of 95°W and the red points
972 indicate sites west of 95°W. The correlation coefficients are shown in (b) and (d). Each
973 point in (b) and (d) represents the mean value for JJA at one specific site. Results for the
974 model and observations are separated out in Fig. S7.

975

Fig. 5. Simulated June-July-August (JJA) summertime average (a) surface [O_3], (b) stomatal conductance, (c) ozone stomatal flux, and (d) damages to GPP at different O_3 sensitivity for 24 U.S. sites. The sites are sorted according to the simulated O_3-free GPP in (d). For each site, the result represents the average over the period when the site GPP measurements are available during JJA. The land cover definitions are: ENF, Evergreen Needleleaf Forest; DBF, Deciduous Broadleaf Forest; SHR, Shrubland; GRA, Grasslands; CRO, Croplands.

Fig. 6. Percentage change in GPP (%) averaged across all sites and grouped by individual PFT type in the presence of different levels of [O_3] as simulated by the YIBs vegetation model. Simulations are performed at 40 NACP sites with a prescribed fixed [O_3] for either low or high O_3 sensitivity. Blue points indicate the average model reduction with the blue horizontal lines indicating the damage range across low to high O_3 sensitivity. The number of sites used to obtain the average reduction value is shown in the title bracket of each subplot. The solid squares with lines show the results (mean plus uncertainty) based on measurements reported in multiple studies. Measurements include: Lombardozzi et al. (2013) for all PFTs; Wittig et al. (2007) for evergreen needleleaf forest (ENF) and deciduous broadleaf forest (DBF); C4 grass or crop (CRO_C4) from Taylor et al. (2002) for spartina alterniflora and Grantz et al. (2012) for sugarcane hybrids; C3 grass or crop (GRA_C3) from Feng et al. (2008) for wheat, Foot et al. (1996) for colluna vulgaris, Mulchi et al. (1992) for soybean, and Ishii et al. (2004) and Ainsworth (2008) for rice. Values for rice are denoted in green and others in red. The author initials are indicated for the corresponding studies.

Fig. 7. Simulated summertime (a) O_3-exposed GPP and (b) O_3 stomatal flux over the U.S. The simulated GPP is overlaid with *in situ* measurements from NACP. The simulations are performed with land cover from ISLSCP and meteorological forcings from MERRA reanalysis. Fig. S8 separates results for model and measurements.

Fig. 8. Simulated reduction fraction in summer GPP in the U.S. due to (a) low and (b) high O_3 sensitivity for 1998-2007.

1007

1008 **Fig. 9.** Simulated changes in summer GPP due to (a, c) 25% reduction or (b, d) 25%

1009 increase in [O_3] for (a, b) low or (c, d) high O_3 sensitivity.

1010
1011

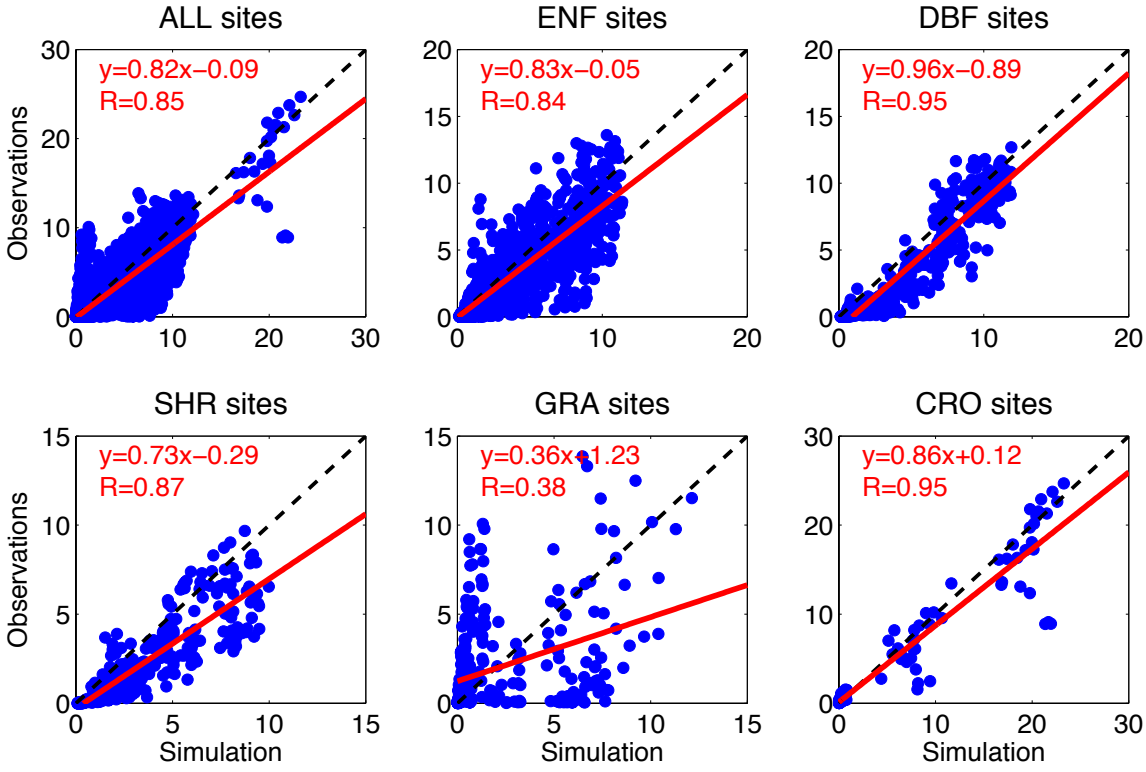

Fig. 1. Comparison between monthly average GPP in the YIBs simulations and NACP observations grouped by PFT type (where *in situ* measurements are available). The red lines indicate linear regression between observations and simulation results. The regression fits and correlation coefficients are shown on each panel. The land types include evergreen needleleaf forest (ENF), deciduous broadleaf forest (DBF), shrublands (SHR), grasslands (GRA), and croplands (CRO). The model-observation comparison for each site is shown in Fig. S4.

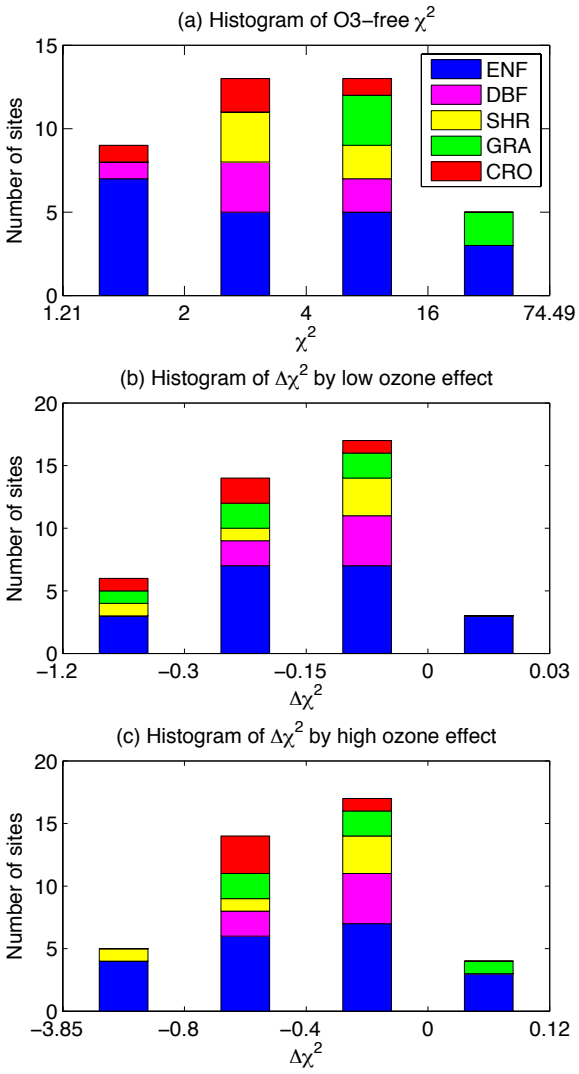

Fig. 2. Histogram of (a) χ^2 for O_3-free GPP and changes in χ^2 after the inclusion of O_3 damage impact with (b) low and (c) high O_3 sensitivity. Each bar represents the number of sites where the χ^2 or $\Delta\chi^2$ of simulations fall between the specific thresholds as defined by the x-axis intervals. The minimum and maximum of χ^2 or $\Delta\chi^2$ are indicated as the two ends of x-axis in the plots. The land cover definitions are: ENF, Evergreen Needleleaf Forest; DBF, Deciduous Broadleaf Forest; SHR, Shrubland; GRA, Grasslands; CRO, Croplands. Results for each site are detailed in Fig. S6.

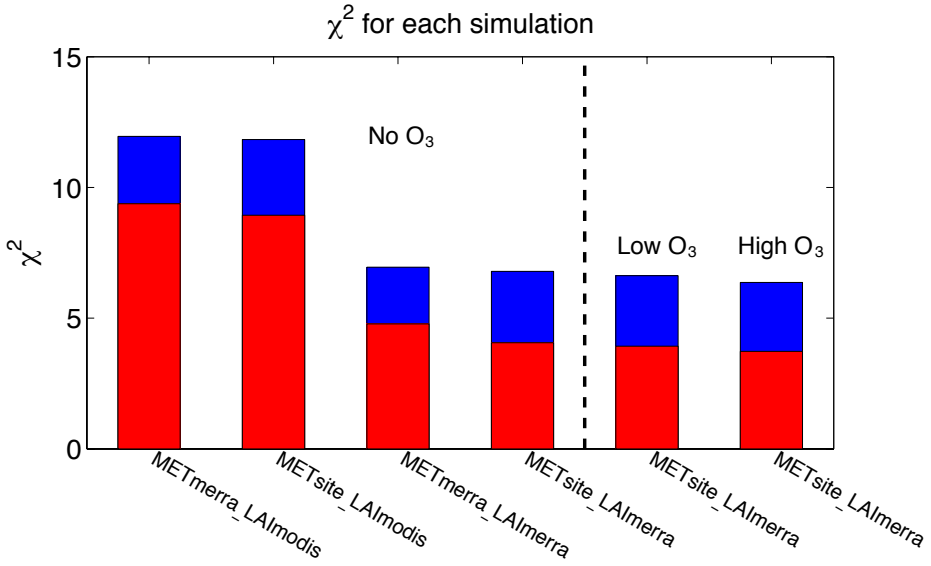

Fig. 3. The calculated average χ^2 of GPP over NACP sites for 6 different simulations as listed in Table 2. The blue bars are results for all 40 NACP sites. The red bars are results excluding sites CA-Let, CA-NS1, US-Var, CA-SJ1, and CA-SJ2, where the simulated site-level χ^2 is larger than 16 as shown in Fig. S6a.

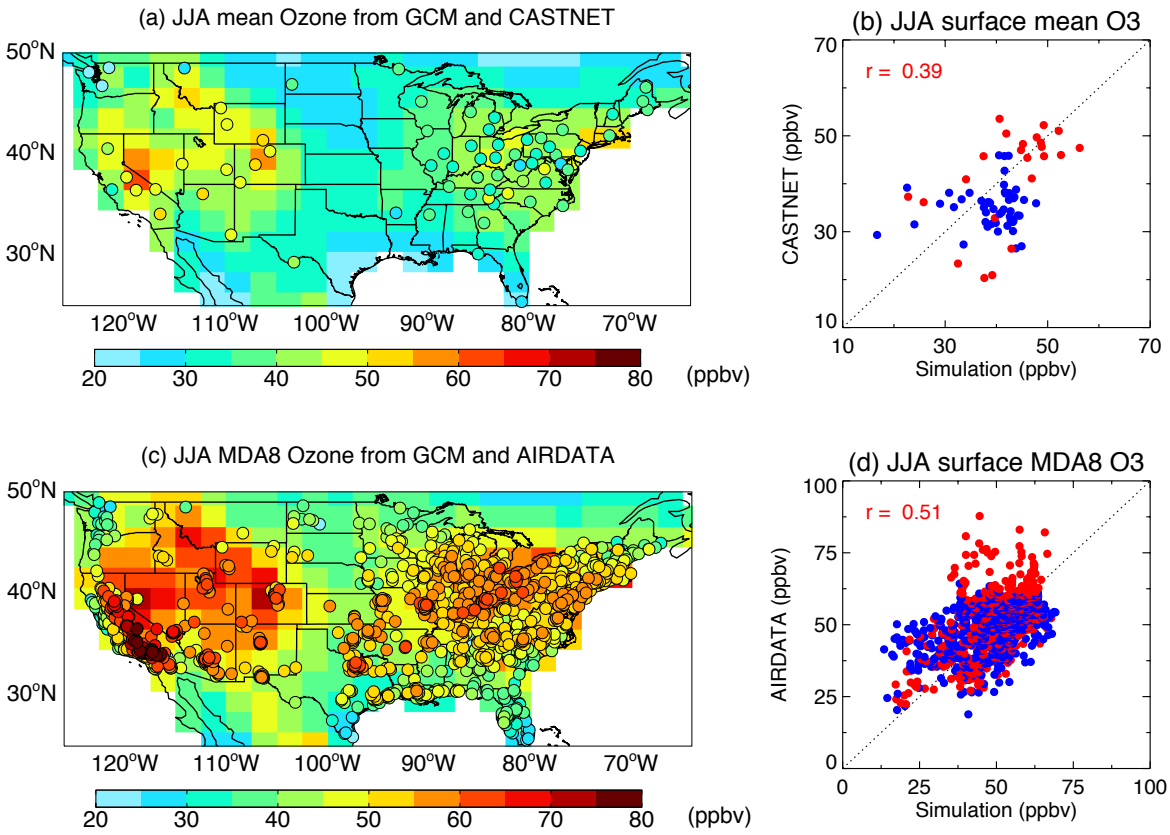

Fig. 4. Validation of simulated June-July-August (JJA) summertime average surface (a, b) diurnal mean and (c, d) daily maximum 8-hour average O_3 with *in situ* measurements from (a, b) the EPA Clean Air Status and Trends Network (CASTNET) and (c, d) the AIRDATA. For (b) and (d), the blue points indicate sites east of 95°W and the red points indicate sites west of 95°W. The correlation coefficients are shown in (b) and (d). Each point in (b) and (d) represents the mean value for JJA at one specific site. Results for the model and observations are separated out in Fig. S7.

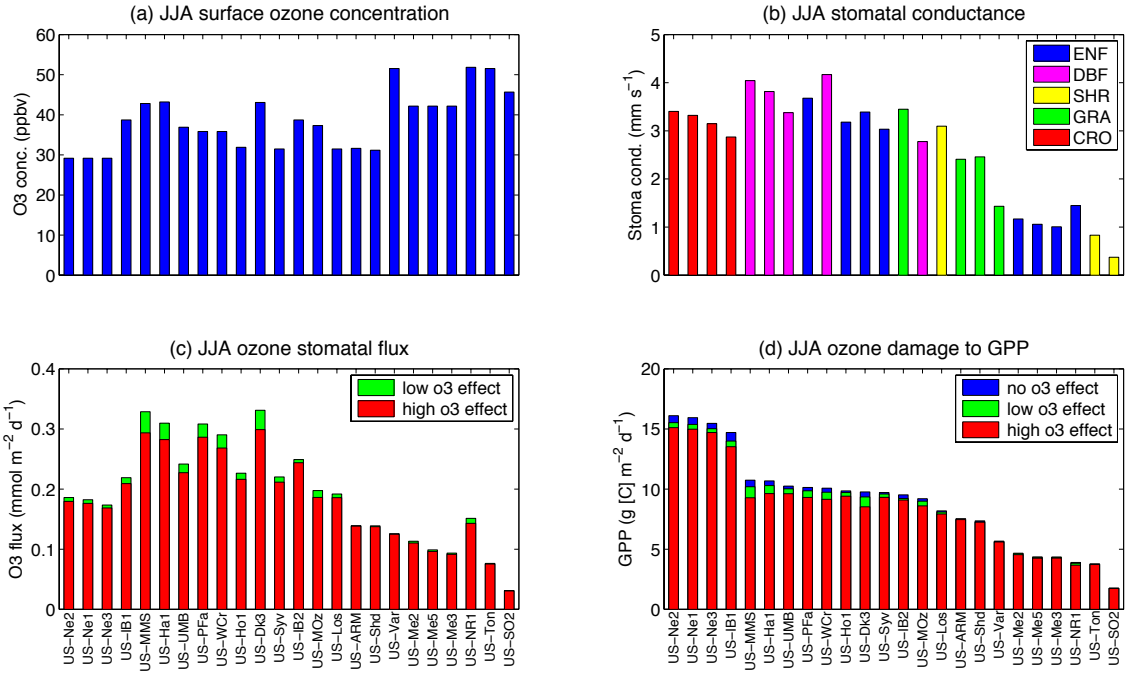

Fig. 5. Simulated June-July-August (JJA) summertime average (a) surface [O_3], (b) stomatal conductance, (c) ozone stomatal flux, and (d) damages to GPP at different O_3 sensitivity for 24 U.S. sites. The sites are sorted according to the simulated O_3-free GPP in (d). For each site, the result represents the average over the period when the site GPP measurements are available during JJA. The land cover definitions are: ENF, Evergreen Needleleaf Forest; DBF, Deciduous Broadleaf Forest; SHR, Shrubland; GRA, Grasslands; CRO, Croplands.

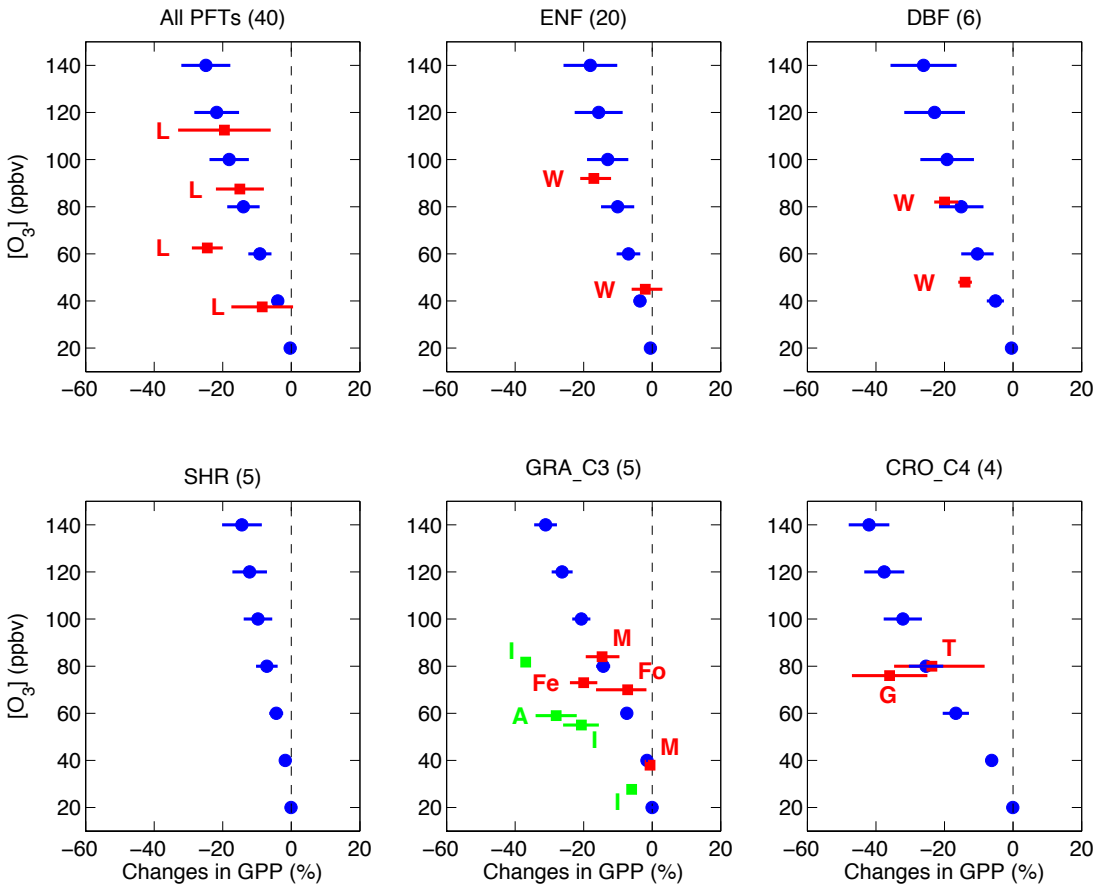

Fig. 6. Percentage change in GPP (%) averaged across all sites and grouped by individual PFT type in the presence of different levels of [O_3] as simulated by the YIBs vegetation model. Simulations are performed at 40 NACP sites with a prescribed fixed [O_3] for either low or high O_3 sensitivity. Blue points indicate the average model reduction with the blue horizontal lines indicating the damage range across low to high O_3 sensitivity. The number of sites used to obtain the average reduction value is shown in the title bracket of each subplot. The solid squares with lines show the results (mean plus uncertainty) based on measurements reported in multiple studies. Measurements include: Lombardozzi et al. (2013) for all PFTs; Wittig et al. (2007) for evergreen needleleaf forest (ENF) and deciduous broadleaf forest (DBF); C4 grass or crop (CRO_C4) from Taylor et al. (2002) for spartina alterniflora and Grantz et al. (2012) for sugarcane hybrids; C3 grass or crop (GRA_C3) from Feng et al. (2008) for wheat, Foot et al. (1996) for colluna vulgaris, Mulchi et al. (1992) for soybean, and Ishii et al. (2004) and Ainsworth (2008) for rice. Values for rice are denoted in green and others in red. The author initials are indicated for the corresponding studies.

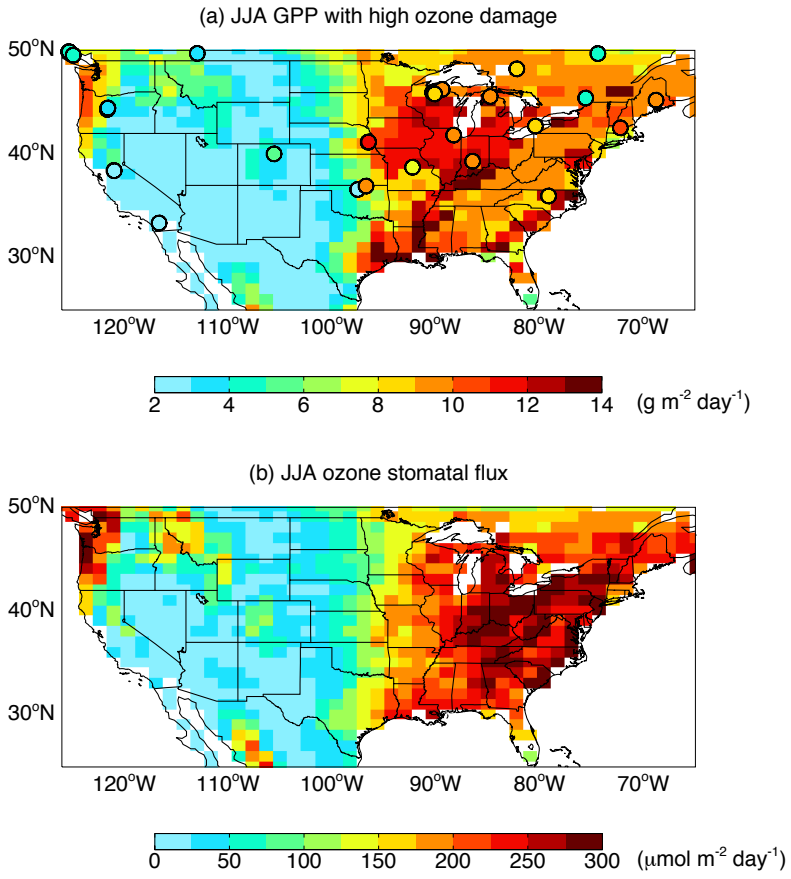

Fig. 7. Simulated summertime (a) O_3-exposed GPP and (b) O_3 stomatal flux over the U.S. The simulated GPP is overlaid with *in situ* measurements from NACP. The simulations are performed with land cover from ISLSCP and meteorological forcings from MERRA reanalysis. Fig. S8 separates results for model and measurements.

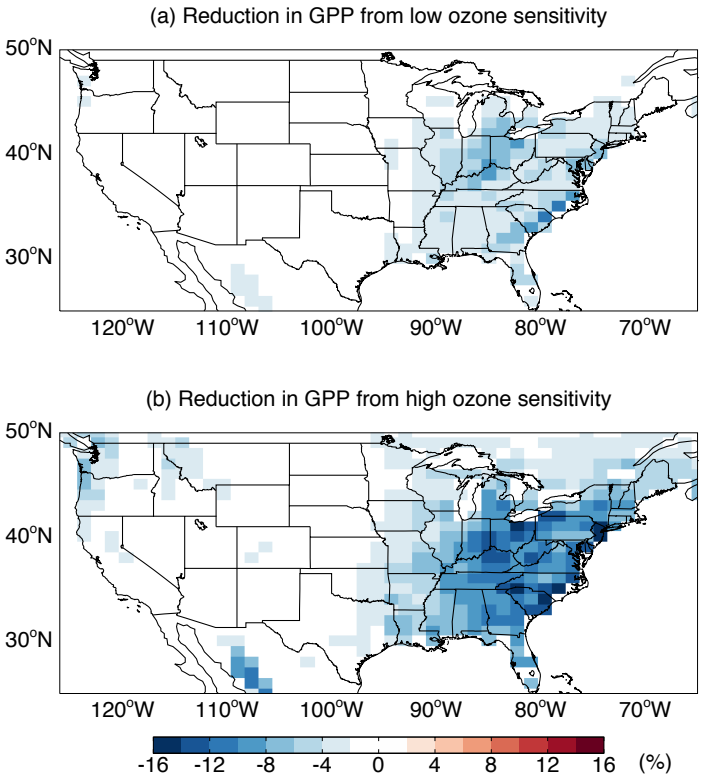

Fig. 8. Simulated reduction fraction in summer GPP in the U.S. due to (a) low and (b) high O_3 sensitivity for 1998-2007.

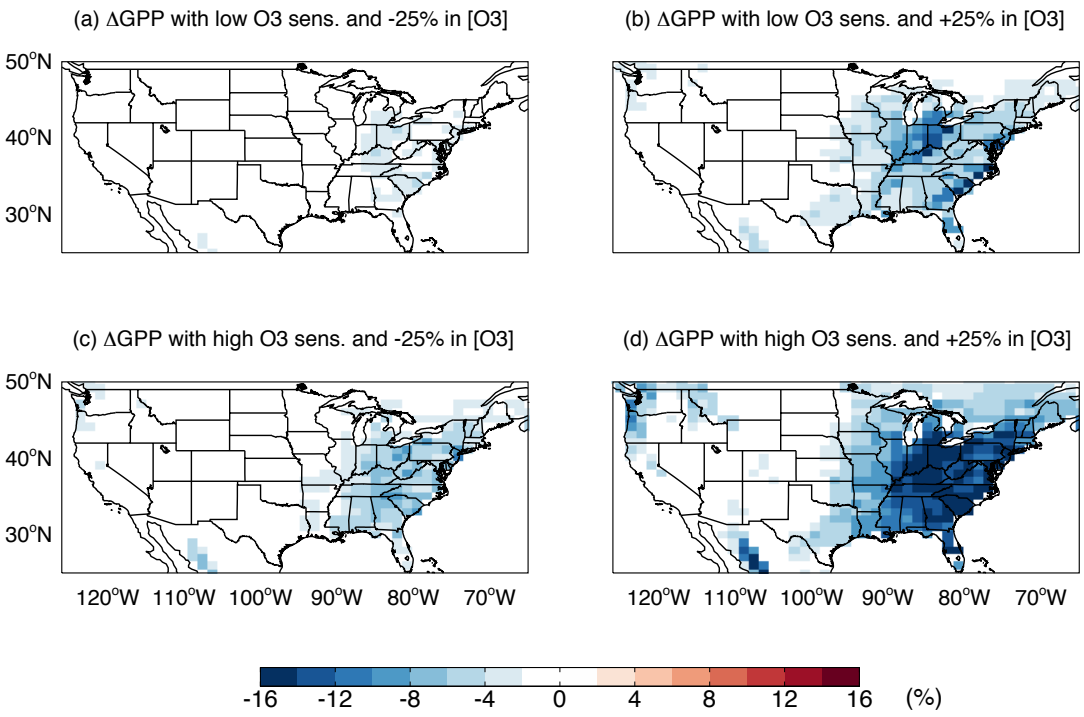

Fig. 9. Simulated changes in summer GPP due to (a, c) 25% reduction or (b, d) 25% increase in [O_3] for (a, b) low or (c, d) high O_3 sensitivity.